

Disentangling the co-evolution of galaxies and supermassive black holes with PRIMA

Bisigello, L.^{1,2*}, Gruppioni³, C., Bolatto A.⁴, Ciesla, L.⁵, Pope, A.⁶, Armus, L.⁷, Smith, J.D.⁸, Somerville, R. S.⁹, Yung, L. Y. A.¹⁰, Wright, R. J.¹¹, Bradford, C. M.^{13,14}, Glenn, J.¹², and Feltre, A.¹⁵

¹ INAF, Istituto di Radioastronomia, Via Piero Gobetti 101, 40129 Bologna, Italy

² Dipartimento di Fisica e Astronomia "G. Galilei", Università di Padova, Via Marzolo 8, 35131 Padova, Italy

³ INAF-Osservatorio di Astrofisica e Scienza dello Spazio, via Gobetti 93/3, I-40129, Bologna, Italy

⁴ Department of Astronomy, University of Maryland, College Park, MD 20742, USA

⁵ Aix Marseille Univ, CNRS, CNES, LAM, Marseille, France

⁶ Department of Astronomy, University of Massachusetts, Amherst, MA 01003, USA

⁷ IPAC, California Institute of Technology, 1200 E. California Boulevard, Pasadena, CA 91125, USA

⁸ Ritter Astrophysical Research Center, University of Toledo, Toledo, OH 43606, USA

⁹ Center for Computational Astrophysics, Flatiron Institute, 162 5th Ave, New York, NY 10010, USA

¹⁰ Space Telescope Science Institute, 3700 San Martin Dr., Baltimore, MD 21218, USA

¹¹ Department of Physics, University of Helsinki, Gustaf Hällströmin katu 2, FI-00014 Helsinki, Finland

¹² NASA Goddard Space Flight Center, Greenbelt, MD 20771, USA

¹³ NASA Jet Propulsion Laboratory, 4800 Oak Grove Dr, Pasadena, CA 91011, USA

¹⁴ California Institute of Technology, 1200 E California Blvd, Pasadena, CA 91125, USA

¹⁵ INAF-Osservatorio Astrofisico di Arcetri, Largo E. Fermi 5, I-50125, Firenze, Italy

ABSTRACT

The most active phases of star formation and black hole accretion are strongly affected by dust extinction, making far-infrared (far-IR) observations the best way to disentangle and study the co-evolution of galaxies and super massive black holes. The plethora of fine structure lines and emission features from dust, ionised and neutral atomic and warm molecular gas in the rest-frame mid- and far-IR provide unmatched diagnostic power to determine the properties of gas and dust, measure gas-phase metallicities and map cold galactic outflows in even the most obscured galaxies. By combining multi-band photometric surveys with low and high-resolution far-IR spectroscopy, the PRobe far-Infrared Mission for Astrophysics (PRIMA), a concept for a far-IR, 1.8m-diameter, cryogenically cooled observatory, will revolutionise the field of galaxy evolution by taking advantage of this IR toolkit to find and study dusty galaxies across galactic time. In this work, we make use of the phenomenological simulation SPRITZ and the Santa Cruz semi-analytical model to describe how a moderately deep multi-band PRIMA photometric survey can easily reach beyond previous IR missions to detect and study galaxies down to $10^{11} L_{\odot}$ beyond cosmic noon and at least up to $z = 4$, even in the absence of gravitational lensing. By decomposing the spectral energy distribution (SED) of these photometrically selected galaxies, we show that PRIMA can be used to accurately measure the relative AGN power, the mass fraction contributed by polycyclic aromatic hydrocarbon (PAH) and the total IR luminosity. At the same time, spectroscopic follow up with PRIMA will allow to trace both the star formation and black hole accretion rates (SFR, BHAR), the gas phase metallicities and the mass outflow rates of cold gas in hundreds to thousands of individual galaxies to $z = 2$.

1. Introduction

Super massive black holes (SMBHs) of millions of solar masses seem to be ubiquitous at the centre of galaxies in the local Universe (e.g. Magorrian et al. 1998; Gültekin et al. 2009; McConnell et al. 2011). Observations have pointed out the presence of relations between the mass of the SMBH and many properties of the host galaxy, such as the stellar mass and the velocity dispersion of the galaxy bulge (Magorrian et al. 1998; Ferrarese 2002), the halo mass (e.g. Ferrarese 2002) and the stellar mass of the host itself (e.g. Mullaney et al. 2012; Reines & Volonteri 2015). The presence of these scaling relations suggests a close evolutionary link between the SMBH and its host galaxy (Kormendy & Ho 2013).

Co-evolution between SMBHs and their host galaxies is also supported by the similarity between the time evolution of the cosmic star-formation-rate density (SFRD; e.g. Gruppioni et al. 2013; Madau & Dickinson 2014; Traina et al. 2024) and of

the black-hole accretion rate density (BHARD; e.g. Delvecchio et al. 2014). Indeed, both quantities show an increase from early epochs up to $z \sim 2 - 3$, followed by a rapid decrease, although these measures are made from disjoint samples. While the rough shape of the SFRD with cosmic time can be understood in the context of merger driven evolution, theoretical models calibrated to reproduce present day scaling relations, seem to produce a wide range in the BHARD at higher redshifts (Habouzit et al. 2020, 2021) due to differences in the implementation of supernovae and black-hole feedback and sub-grid physics.

Observationally, the study of both the SFRD and the BHARD is hampered by the presence of dust, as the most active phases of black hole growth and star formation are heavily enshrouded. Indeed, the contribution of the dust-obscured SFRD to the total is above 50% at least up to $z = 4$ (Zavala et al. 2021, Traina et al. in prep.). Moreover, some galaxies are so obscured by dust to be detectable in the infrared (IR), but faint or totally missed at optical wavelengths (e.g. Gruppioni et al. 2020; Talia

* e-mail: laura.bisigello@inaf.it

et al. 2021; Rodighiero et al. 2023; Bisigello et al. 2023; Pérez-González et al. 2023).

Herschel results showing that the majority of IR galaxies with $L_{\text{IR}} > 10^{11} L_{\odot}$ at $z > 1$ host a low-luminosity or obscured AGN (AGN; Gruppioni et al. 2013; Magnelli et al. 2013) support the hypothesis of SMBHs and galaxies co-growth and co-evolution, and therefore the need to observe the peak of their activity (i.e., cosmic noon) in the IR. Similarly, recent *James Webb Space Telescope* (JWST) observations of numerous faint, broad-line AGN at $z > 5$ (e.g. Onoue et al. 2023; Kocevski et al. 2023; Harikane et al. 2023; Larson et al. 2023), possibly pointing to Eddington-limited accretion onto massive black hole seeds formed at $z > 15$ (e.g., Maiolino et al. 2023). At the same time, about 20% of the broad-line AGN identified with JWST appear as red and compact sources, with a steep red continuum in the rest-frame optical and a blue/flat continuum in the rest-frame ultraviolet (UV) (e.g. Kocevski et al. 2023, 2024; Harikane et al. 2023; Matthee et al. 2024; Greene et al. 2023; Killi et al. 2023). Despite the AGN signature in the rest-frame optical, the majority of these so called ‘little red dots’ are weak or undetected X-ray emission with Chandra (Yue et al. 2024). These objects could be heavily obscured by dust heated by buried AGN (e.g. Kocevski et al. 2023; Matthee et al. 2024; Greene et al. 2023), very compact starbursts with large numbers of OB stars (e.g., Pérez-González et al. 2024), Compton thick AGN with a dust-poor medium or intrinsically X-ray weak AGN, such as Narrow Line Seyfert 1s (Maiolino et al. 2024).

Given the observational and theoretical evidence that galaxies and their SMBH grow together, and that the most rapid growth occurs during phases that are hidden by dust (Hickox & Alexander 2018), it is essential to measure SFR and BHAR in high- z populations using tools that are insensitive to the effects of dust obscuration. It is also important to perform these studies in the same populations of galaxies, where observation biases can be well understood and selection effects minimised. The rest frame mid- and far-IR spectrum offers a plethora of fine structure gas lines and emission features from dust and warm molecular gas that are sensitive to AGN and star-formation (SF) activity (Fig. 1) and are not (or very little) affected by dust-extinction. In particular, among the AGN tracers there are [Ne v] at 14.3 and 24.3 μm , [O iv] at 24.9 μm and [Ne iii] at 15.7 μm (e.g. Rigby et al. 2009; Fernández-Ontiveros et al. 2016; Feltre et al. 2023). At the same time, Polycyclic Aromatic Hydrocarbon (PAH) emission features present between 3 and 20 μm , the mid-IR pure rotational lines of H₂ at 17 μm , low-ionisation fine structure lines like the [Ne ii] line at 12.8 μm , the [S iii] lines at 18 and 33 μm , or the [C ii] line at 158 μm (e.g. De Looze et al. 2014; Vallini et al. 2015) are sensitive tracers of star formation. While some of these lines are excited by both star formation and AGN activity, it has been shown that the relative contributions can be decomposed (Stone et al. 2022). Many of these lines have already been used in the Local Universe to study the SFR and the BHAR in individual bright IR galaxies (e.g. Armus et al. 2004, 2006, 2007, 2023; Spinoglio et al. 2015, 2022; Spoon et al. 2009; Díaz-Santos et al. 2013; Inami et al. 2013; Stierwalt et al. 2014; Lai et al. 2022; Stone et al. 2022), but cold sensitive far-IR observatories are necessary to extend these studies to higher redshifts and to less extreme galaxies.

Dust grains play a crucial role on the formation and cooling of molecular gas and, therefore, on the formation of new stars (Draine 2003; Peimbert & Peimbert 2010). For this reason, theoretical models predict that the dust abundance and metallicity of the interstellar medium (ISM) should be closely related (Zhukovska 2014), as a large fraction of metals is converted into

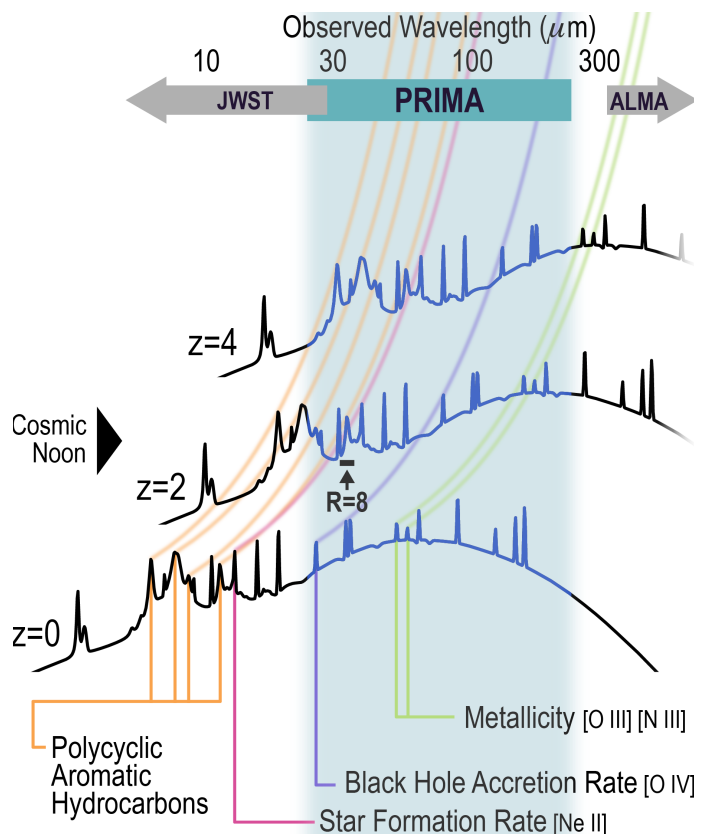


Fig. 1. The mid- and far-IR spectra of galaxies contains a plethora of features useful to derive SFR, BHAR and metallicity. The observed wavelengths of some of these tracers are reported in the figure, together with the SED of an example star-forming galaxy at $z = 0$, $z = 2$ and $z = 4$, taken from Moullet et al. (2023, section 47) We also highlight the wavelength coverage of JWST, PRIMA (shaded region) and ALMA.

dust when they are injected into the ISM by asymptotic giant branch stars and supernovae. At the same time, the rate of dust destruction by supernova blast waves is thought to be an order of magnitude higher than dust production by dying stars (Dwek & Cherchneff 2011). There is clearly a large gap in our knowledge of dust formation (and star-formation as a consequence) and destruction, which can be solved only by tracing both metals and dust in the same galaxies. PAHs features, present in the rest-frame mid-IR, are both tracers of star-formation and sensitive tracers of the abundance of small carbonaceous dust grains. At the same time, in dusty galaxies gas metallicity can be measured using bright, far-IR tracers such as [N iii]57 μm , [O iii]52 μm and [O iii]88 μm (Nagao et al. 2011; Pereira-Santaella et al. 2017; Fernández-Ontiveros et al. 2017), which are unaffected by dust extinction and have a negligible dependence on the gas temperature, unlike their optical and UV counterparts (e.g., Bernard Salas et al. 2001).

To fully understand the interplay between AGN and their host galaxies, it is also necessary to identify and measure galactic outflows, a powerful form of feedback that can inject significant amounts of energy into the ISM, and drive gas and dust into the circumgalactic medium (CGM). Outflows are invariably multi-phase, but the cold ($T < 10^4 \text{K}$) component often dominates the gas mass (Veilleux et al. 2020). Spectroscopic observations of strong absorption features in the far-IR, such as OH, can be used to estimate the outflow velocity and mass outflow rate (González-Alfonso et al. 2014, 2017). Observations of cold outflows using OH absorption lines have been very effective,

indicating large masses of outflowing dense gas that can rival or exceed the star formation rate in ultra-luminous IR galaxies (González-Alfonso et al. 2017), although detailed studies have so far been limited to small numbers of galaxies in the Local Universe (see Veilleux et al. 2020, for a review). Sensitive, cold far-IR spectroscopic observatories that can reach levels significantly fainter than were possible with *Herschel* are necessary to carry these studies to high-redshifts and trace cold outflows to cosmic noon and beyond in statistically significant samples of normal galaxies.

The PRobe far-Infrared Mission for Astrophysics, PRIMA¹ (P.I. J. Glenn), is a concept for a far-IR, cryogenically cooled observatory with an 1.8 m diameter. PRIMA's current design includes two science instruments: FIRESS and PRIMAgger. FIRESS is a powerful, multi-mode survey spectrometer covering wavelengths between 24 and 235 μm and having two different spectral modes, a low-resolution mode with $R \sim 100$ and a high-resolution FTS mode which offers tunable spectral resolution up to $R = 4,400$ at 112 μm and 20,000 at 25 μm . PRIMAgger is a multiband spectro-photometric imager that offers hyper-spectral linear variable filters in two bands ($R = 10$, PHI1 and PHI2) from 24 to 80 μm together with polarimetric capabilities in four broadband filters (PPI) between 80 and 261 μm . Because it is cooled, and uses state of the art kinetic inductance detectors (e.g., Day et al. 2003, 2024; Baselmans 2012), PRIMA is orders of magnitude more sensitive than previous far-IR space missions. PRIMA is designed to rapidly survey the IR sky, achieving mapping speeds 3-5 orders of magnitude faster than its far-IR predecessors. In this work we outline the revolutionary role that PRIMA will play in studying galaxy and AGN co-evolution across cosmic time. Although here we illustrate the power of PRIMA by describing possible deep and wide surveys and follow-up spectroscopy with PRIMAgger and FIRESS, we must stress that PRIMA is a true community observatory, with at least 75% of the observing time available to astronomers through a traditional, peer-reviewed, General Observers program (for an overview of different general observers science cases see Moullet et al. 2023). Moreover, all PI data will be publicly available to Guest Investigators.

The paper is organised as follows. In Sect. 2 we present the PRIMA example surveys together with the simulations used in the analysis. In Sect. 3 we discuss the SFR, BHAR, metallicity and outflows measurements, using both photometric and spectroscopic IR observations. We finally report and summarize our conclusions in Sect. 4. Throughout the paper, we consider a ΛCDM cosmology with $H_0 = 70 \text{ km s}^{-1} \text{ Mpc}^{-1}$, $\Omega_m = 0.27$, $\Omega_\Lambda = 0.73$, and a Chabrier initial mass function (IMF, Chabrier 2003).

2. Methods

To assess the capability of PRIMA to disentangle galaxy and AGN evolution as well as to measure metallicity and cold outflows, we have made use of the spectro-photometric realisations of infrared-selected targets at all- z (SPRITZ² v1.13; Bisigello et al. 2021, 2022) and the Santa Cruz semi-analytic model (SC SAM; Somerville et al. 2015). In the next sections we give some brief details on the PRIMAgger instrumental capabilities, on these two simulations, and explain how it is possible to measure both SFR and BHAR using far-IR spectro-photometric data.

Table 1. PRIMAgger filter bandpasses and survey depths.

Filter	λ_{cen} [μm]	Conservative		Payload	
		Deep $f_{5\sigma}$ [μJy]	Wide $f_{5\sigma}$ [μJy]	Deep $f_{5\sigma}$ [μJy]	Wide $f_{5\sigma}$ [μJy]
PHI1_1	25.0	70.8	233.9	75.0	233.3
PHI1_2	27.8	78.7	249.2	83.1	258.5
PHI1_3	30.9	87.6	277.0	92.7	288.4
PHI1_4	34.3	99.0	312.9	102.9	320.1
PHI1_5	38.1	113.0	358.9	114.3	355.6
PHI1_6	42.6	134.2	424.2	126.9	394.8
PHI2_1	47.4	82.9	262.1	141.0	438.7
PHI2_2	52.3	94.3	298.2	156.9	488.1
PHI2_3	58.1	108.4	342.9	174.3	542.3
PHI2_4	64.5	123.2	389.6	193.5	602.0
PHI2_5	71.7	152.5	482.3	215.1	669.2
PHI2_6	79.7	172.1	544.3	239.1	743.9
PPI1	96.3	28.6	90.4	276.0	858.7
PPI2	126.0	44.9	142.0	378.0	1176.0
PPI3	172.0	67.0	211.7	516.0	1605.0
PPI4	235.0	81.6	258.2	705.0	2193.3

Notes. In the table we report the PRIMAgger filter bandpasses with their respective central wavelength and 5σ depths in the Deep and Wide surveys considered in this work. Both surveys correspond to 1500h, but spread over 1 deg^2 for the Deep and 10 deg^2 for the Wide. We report both the conservative expectation survey depths (conservative) and the guaranteed payload requirement depths (payload), both excluding confusion. Note that PHI provides $R = 10$ continuous spectral coverage, which we here represent as discrete filters, or bands, to make the calculations more tractable.

2.1. PRIMA surveys

As example cases, we considered two different designs for the PRIMAgger surveys. Both surveys have a total observing time of 1500h, distributed over 1 deg^2 for the Deep survey and over 10 deg^2 for the Wide survey. In the rest of the paper, we consider a galaxy as detected if it has a $S/N > 5$ in half of the PRIMAgger hyper-spectra filters (PHI), to assure good description of the overall far-IR spectral energy distribution (SED) and limiting problems due to confusion. In Tab. 1 we list the PRIMAgger filters and the depths considered for the Deep and Wide surveys. As reference we use the conservative depths, taking into account that the instrument current best estimate (CBE) is better than this conservative expectations by a factor of ~ 1.7 in the hyper-spectra PHI bands and ~ 2 in the long wavelengths PPI filters. However, when necessary, we also make comparison with the payload limits, which are the guarantee requirement payload depths. Although the hyper-spectra filters PHI band of PRIMAgger will provide continuous, highly over-sampled spectra at $R = 10$ from 24 to 80 μm , we assume in the following that this band is composed of 12 top-hat filters with an $R = 10$. Similarly, we represent the four PRIMAgger broad band filters (PPI) as continuous rectangular filters spanning the wavelength range of the band, i.e. $R = 4$.

From these photometric surveys it will be possible to select a sub-sample of sources to follow-up spectroscopically with FIRESS. In particular, with one hour of integration time we expect to detect lines with fluxes above 10^{-19} W/m^2 with the low-resolution mode of FIRESS. As shown in Fig. 2, we expect the number of observed spectroscopic sources to be well below the limit of 15 sources per beam per resolution element, above which we expect PRIMA could be affected by line confusion. We

¹ <https://prima.ipac.caltech.edu/>

² <http://spritz.oas.inaf.it/>

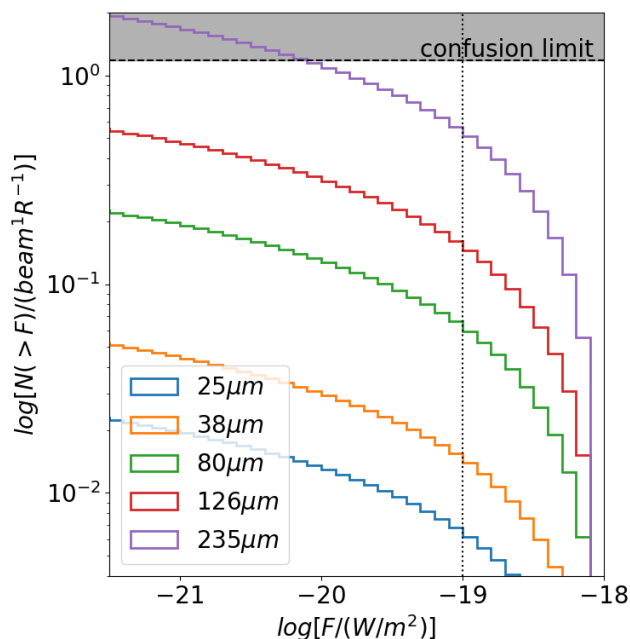


Fig. 2. We do not expect FIRESS to be affected by line confusion down to at least 10^{-20} W/m^2 . We show the cumulative line number counts per beam and resolution element at different wavelengths, as derived using SPRITZ. The vertical dotted line shows the flux of 10^{-19} W/m^2 , reachable with FIRESS with one hour of integration time. The horizontal dashed line and the shaded region show the limit of $15/\text{beam}/R$, above which PRIMA could be affected by line confusion at the longest wavelengths.

note that these line counts do not include the effects of confusion which could increase line blending in some cases. However, at the depth of 10^{-19} W/m^2 , FIRESS should not be largely affected by line confusion, even at the longest observed wavelength (i.e. $235 \mu\text{m}$). This is true even down to a depth of 10^{-20} W/m^2 .

2.2. SPRITZ

The SPRITZ simulation is particularly well suited to predictions for PRIMA as it starts from previously observed IR luminosity functions (Gruppioni et al. 2013) of star-forming galaxies, AGN and composite systems. These are complemented by the K-band luminosity function of elliptical galaxies and the galaxy stellar mass function of dwarf irregulars. These functions are used in SPRITZ to derive the number of galaxies expected at different redshifts ($z = 0 - 10$) and IR luminosities ($\log_{10}(L_{\text{IR}}/L_{\odot}^{-1}) = 5 - 15$). The galaxies included in the simulations can be broadly grouped into four populations:

- Star-forming galaxies correspond to star-forming galaxies with no evident sign of AGN activity. This class includes spirals and starbursts, as derived from the observed *Herschel* IR luminosity functions (Gruppioni et al. 2013), dwarf irregulars, derived from their observed galaxy stellar mass function (Huertas-Company et al. 2016; Moffett et al. 2016). Spirals have specific star-formation rates $\log(\text{sSFR}/\text{yr}^{-1}) = -10.4$ to -8.9 , while starbursts have higher sSFR ranging from $\log(\text{sSFR}/\text{yr}^{-1}) = -8.8$ to -8.1 . Dwarf irregulars are instead galaxies with lower stellar masses, as their characteristic stellar mass (i.e., mass at the knee of the mass function) is $\log_{10}(M_*/M_{\odot}) \leq 11$.
- AGN-dominated systems are galaxies whose mid-IR emission is dominated by AGN activity. They include two dif-

ferent populations which differ by their optical extinction, i.e. AGN1 and AGN2. Their number densities have been derived by Bisigello et al. (2021) combining the observed AGN IR and UV observed luminosity functions (Gruppioni et al. 2013; Croom et al. 2009; McGreer et al. 2013; Ross et al. 2013; Akiyama et al. 2018; Schindler et al. 2019).

- Composite systems are objects whose energetics are dominated by star formation, but which include a faint AGN component. They are split into star-forming AGN (SF-AGN), which have an intrinsically faint AGN (i.e., $L_{\text{BOL}} \leq 10^{13} L_{\odot}$), and SB-AGN, whose AGN is bright but extremely obscured (i.e., $\log(N_{\text{H}}/\text{cm}^{-2}) = 23.5 - 24.5$). Both populations are derived starting from the observed *Herschel* luminosity function (Gruppioni et al. 2013).
- Passive galaxies are elliptical galaxies, generally with little or no star-formation, as derived from the observed K-band luminosity functions (Arnouts et al. 2007; Cirasuolo et al. 2007; Beare et al. 2019). Some of these galaxies may host an obscured AGN.

To each simulated galaxy we assign one SED model that depends on its galaxy population (Polletta et al. 2007; Rieke et al. 2009; Gruppioni et al. 2010; Bianchi et al. 2018) in order to derive the photometric fluxes expected in different filters, spanning from UV to radio wavelengths. The proportions of galaxies belonging to each population is derived by the luminosity function evolution of the different galaxy classes, at different redshifts and luminosities. We then fit the empirical SED assigned to each simulated galaxy using the software SED3FIT (for AGN; Berta et al. 2013), in order to disentangle the AGN from the galaxy contribution, or the multi-wavelength analysis of galaxy physical properties MAGPHYS (for non-active objects; da Cunha et al. 2008). From the fit we retrieved the stellar mass, the accretion luminosity, the hydrogen column density of the dusty torus, and the contributions to the IR luminosity of star-formation and AGN activity. The SFR is directly taken from the UV continuum and the IR luminosity, for the unobscured and obscured components, respectively. We then used several theoretical and empirical relations to derive additional physical properties, which are marginally or not constrained from the SED fitting, such as the X-ray AGN luminosity and the metallicity.

The simulation also includes IR emission lines due to star-formation or AGN activity associated to the SEDs through several empirical relations (e.g. Bonato et al. 2019; Gruppioni et al. 2016). In the next section we report some update required to take into account the dependence on metallicity of some key IR lines.

Overall, SPRITZ is consistent with a large set of observations from $z = 0$ to $z = 6$. This includes luminosity functions and number counts at different redshifts from X-rays to radio, the total galaxy stellar mass function, the molecular gas mass density, the CO and [CII] luminosity functions (Bisigello et al. 2022), AGN diagnostic diagrams (Euclid Collaboration: Bisigello et al. 2024), and the SFR versus stellar mass plane. We refer to Bisigello et al. (2021, 2022) and Euclid Collaboration: Bisigello et al. (2024) for further comparisons with observations and more details on the SPRITZ simulation.

Linking far-IR lines to gas metallicity in SPRITZ

Rest frame mid- and far-IR emission lines are included in the SPRITZ simulation using the empirical relations by Bonato et al. (2019) and Gruppioni et al. (2016), linking the line luminosity to L_{IR} . However, future IR facilities, such as PRIMA, with sensitive spectral capabilities can take advantage of metal-sensitive far-IR

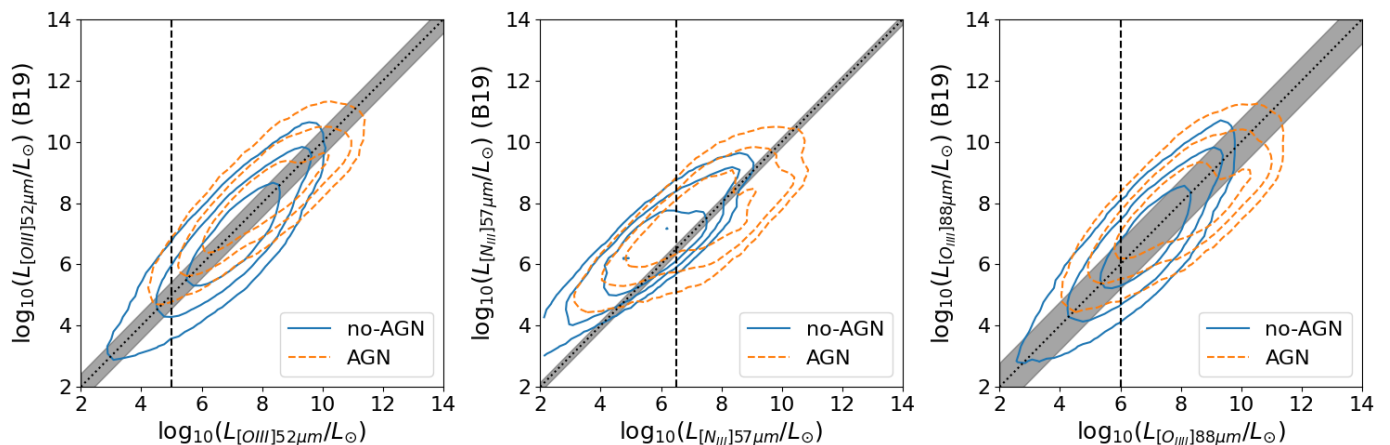


Fig. 3. The metallicity-dependent method outlined in Sect. 2.2 gives luminosity estimates consistent with those derived using the empirical relations by (Bonato et al. 2019). In the figure we show the comparison for the $[\text{O III}]52\mu\text{m}$ (left), $[\text{N III}]57\mu\text{m}$ (center) and $[\text{O III}]88\mu\text{m}$ (right) lines. Dotted lines indicate a 1:1 relation, with the shaded region showing the 1σ of the relations by (Bonato et al. 2019). The vertical dashed lines show the minimum line luminosity used in the relation by (Bonato et al. 2019). Contours correspond to 68%, 95% and 99.7% of the distribution of objects hosting an AGN (orange dashed contours) and non active galaxies (solid blue contours).

lines including $[\text{N III}]57\mu\text{m}$, $[\text{O III}]52\mu\text{m}$ and $[\text{O III}]88\mu\text{m}$ to trace gas metallicity. For this reason we implement an alternative approach to estimate the strengths of these key far-IR lines in the galaxies modeled with SPRITZ.

As demonstrated by Lamarche et al. (2022), the absolute O/H abundance can be derived directly from the far-IR cooling lines $[\text{O III}]52\mu\text{m}$ and/or $[\text{O III}]88\mu\text{m}$ measurements, when supplemented with a tracer of hydrogen emission measure (recombination or free-free emission). The *relative* abundance measure N/O is also of strong interest, since nitrogen undergoes enhancement relative to oxygen from secondary production in CNO cycle stars. The N/O abundance has been established to correlate well with absolute abundance locally (Nagao et al. 2011; Pereira-Santaella et al. 2017; Spinoglio et al. 2022), revealing significant discrepancies with optical abundance measure in dusty local systems (Peng et al. 2021; Chartab et al. 2022).

To incorporate realistic luminosities for abundance-sensitive lines, we start by incorporating the $[\text{O III}]88\mu\text{m}$ line using the analytical model by Yang & Lidz (2020), which links the $[\text{O III}]88\mu\text{m}$ luminosity directly to the gas metallicity (Z) and the SFR:

$$\frac{L_{[\text{O III}]88\mu\text{m}}}{L_{\odot}} = 10^{8.27 - 0.0029(7.3 + \log(Z/Z_{\odot}))^{2.5}} \frac{Z}{Z_{\odot}} \frac{\text{SFR}}{M_{\odot}/\text{yr}} \quad (1)$$

where Z_{\odot} indicated the solar value.

The ratio between the $[\text{O III}]52\mu\text{m}$ and $[\text{O III}]88\mu\text{m}$ line is a strong function of the electron density n_e (e.g., Draine 2011). In SPRITZ, we randomly assign an electron density n_e between 10^2 and 10^3 cm^{-3} to each galaxy and derive the $[\text{O III}]52\mu\text{m}$ expected luminosity directly from the $[\text{O III}]88\mu\text{m}$ luminosity. These electron densities are consistent with measurements obtained using mid and far-IR density-sensitive tracers in local Universe systems spanning moderate to very high specific SFRs (e.g., Dale et al. 2006; Inami et al. 2013; Herrera-Camus et al. 2016).

From the metallicity and the respective oxygen abundance, we retrieved the expected nitrogen abundance, as quantified in the local universe using observations of late type galaxies by Pilyugin et al. (2014):

$$12 + \log(N/H) = 2.47(12 + \log(O/H)) - 13.43 \quad (2)$$

if $12 + \log(O/H) \geq 8.1$

$$12 + \log(N/H) = 0.96(12 + \log(O/H)) - 1.20$$

if $12 + \log(O/H) < 8.1$

We then made use of this information to estimate the nitrogen to oxygen abundance ratio (N/O). This allowed us to predict the $[\text{N III}]57\mu\text{m}$ luminosity from the $[\text{O III}]52\mu\text{m}$ line, assuming an electron density of 10^4 cm^{-3} (near both lines' critical densities) and a temperature of 10^4 K

$$\frac{L_{[\text{N III}]57\mu\text{m}}}{L_{[\text{O III}]52\mu\text{m}}} = \frac{N}{O} \frac{1}{0.4} \frac{1.0 + 0.377x + 0.0205x^2}{1.0 + 0.691x + 0.0966x^2} \quad (3)$$

where $x = n_e / \sqrt{T}$ (Peng et al. 2021).

The above methods allow us to derive the line luminosity powered by stellar activity, however, all three lines can be also powered by AGN activity. In order to include this contribution, we used the models from Feltre et al. (2016), computed with the photoionization code CLOUDY (v13.03, Ferland et al. 2013). In particular, we consider a ionisation parameter at the Strömgen radius randomly varying between $\log_{10}(U_S) = -1.5$ and -3.5 , a range of sub- and super-solar interstellar metallicity (0.008, 0.017, 0.03), a UV spectral index $\alpha = -1.4$, a dust-to-metal ratio of 0.3 and internal micro-turbulence velocity $v = 100 \text{ km/s}$ (see Mignoli et al. 2019). The hydrogen number density is assumed to be 10^3 cm^{-3} .

In Figure 3 we show the comparison between these line flux estimates and the empirical relation presented in Bonato et al. (2019). The estimates for $[\text{O III}]52\mu\text{m}$ and $[\text{O III}]88\mu\text{m}$ are largely consistent with the empirical relations. The estimated $[\text{N III}]57\mu\text{m}$ line luminosity, however, while consistent for AGN and composite objects, is on average around 1 dex below the empirical relation for purely star-forming objects. These line luminosities, however, are well below the luminosity range traced by the observations used in (Bonato et al. 2019). Similar results, although with a larger scatter, are obtained if we consider the line luminosities obtained using the empirical relations by (Gruppioni et al. 2016). We conclude therefore, that for the purposes of

predicting PRIMA detection rates, the estimated line luminosities of $[\text{O III}]52\mu\text{m}$, $[\text{O III}]88\mu\text{m}$ and $[\text{N III}]57\mu\text{m}$ in SPRITZ used here, which include a realistic dependence on metallicity, are generally consistent with previous observations.

2.3. Santa Cruz SAM

In addition to SPRITZ, we have made use also of the state-of-the-art Santa Cruz semi-analytic model (SC SAM Somerville et al. 2015). For the purpose of this work, we utilised five simulated past lightcones presented by Yung et al. (2023), each covering an area of 2 deg^2 and spanning a redshift range of $0 < z \lesssim 10$. These lightcones are constructed with halos extracted from the dark matter-only cosmological SMDPL simulation from the MultiDark suite, which has a volume of $(400 \text{ Mpc } h^{-1})^3$ and reliably resolves halos down to $M_h \sim 10^{10} M_\odot$ (Klypin et al. 2016). For halos in a lightcone, Monte Carlo realisations of dark matter halo merger histories are constructed using an extended Press-Schechter (EPS)-based algorithm (e.g. Somerville & Kolatt 1999), which provides input for the SC SAM described below. We refer the reader to Yung et al. (2022) and Somerville et al. (2021) for details regarding the constructions of lightcones.

The galaxies and AGN in the lightcones are simulated with the versatile and well-established SC SAM (Somerville & Primack 1999; Somerville et al. 2008, 2015), which models the formation and evolution of large ensembles of galaxies by tracking the flows of mass and metals into and out of the intergalactic medium, galaxy halos, and galaxies. These flows are driven by physical processes occurring across a vast range of scales, including gas accretion from the cosmic web into halos, cooling from the circumgalactic medium into cold gas reservoirs within galaxies, BH accretion in the centres of galaxies, and large-scale galactic outflows driven by supernovae and AGN feedback. The SAM provides predictions for a wide range of physical properties, including stellar mass, SFR, black hole mass, and BHAR (Somerville et al. 2021; Yung et al. 2019a). The simulated galaxy populations in the lightcones are complete down to $M_* \sim 10^7 M_\odot$. With physical parameters calibrated to a subset of observed galaxy properties at $z \sim 0$, the SAM is able to reproduce the evolution of many observational quantities, including multi-wavelength luminosity functions up to $z \sim 10$, one-point distribution functions of stellar mass and SFR up to $z \sim 8$, and various scaling relations (Somerville et al. 2015, 2021; Yung et al. 2019a,b). The spatial distribution of sources in the lightcone are in excellent agreement with the observed two-point angular correlation functions (Yung et al. 2022). In addition, the model has also been shown to reproduce the observed evolution in AGN bolometric, UV, and X-ray luminosity functions up to $z \sim 5$ (Hirschmann et al. 2012; Yung et al. 2021).

2.4. Deriving SFR and BHAR from far-IR spectro-photometric data

SEDs that extend from approximately $15 \mu\text{m}$ to $150 \mu\text{m}$ in the rest frame can be used to reliably determine the respective importance of star formation and black hole accretion activity (Kirkpatrick et al. 2015; Ciesla et al. 2015; Gruppioni et al. 2015), as shown in Fig. 4. This tends to work because the AGN contributes primarily to warm dust that emits in the rest frame mid-IR range peaking around $20 \mu\text{m}$, while star formation activity creates a colder dust component which dominates the far-IR, peaking around $100 \mu\text{m}$ (Shimizu et al. 2017).

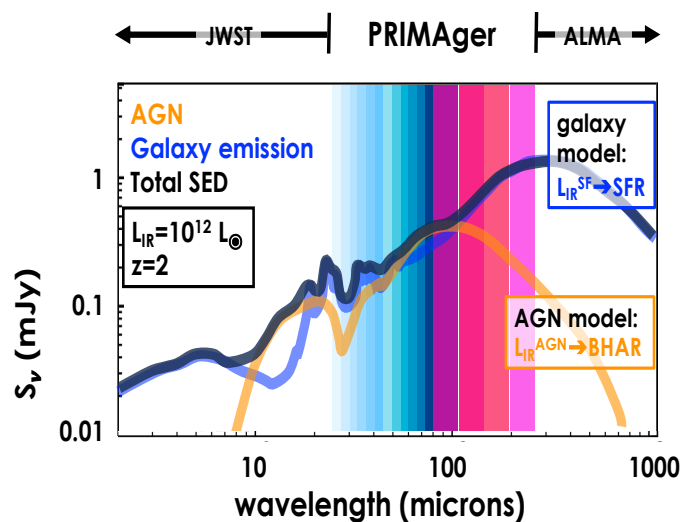


Fig. 4. Example of SED decomposition for an $L_{\text{IR}}=10^{12}$ galaxy at $z=2$. Star formation (blue), and AGN heated dust (orange), are shown schematically here and combine to produce a composite galaxy SED (black) that can be decomposed using the PRIMAger bands, shown here in different colours, from pale blue to magenta.

Studies based on SED decomposition show that the warm dust temperature, the colour temperature and the relative luminosity of the cold and warm components are all excellent indicators of the fraction of power contributed by the AGN in the mid-IR and bolometrically (Kirkpatrick et al. 2015). For highly obscured galaxies, such as those prevalent at $z \sim 1 - 2$, dust luminosity is an excellent proxy for the bolometric luminosity of the system. Thus warm dust mid-IR luminosities can be used to directly compute the bolometric luminosity of the AGN ($L_{\text{bol}}^{\text{AGN}}$). Indeed, as shown for example by (Gruppioni et al. 2016) and reported in Fig. 5 using a sample of local AGN, the AGN bolometric luminosity derived through SED-fitting and decomposition is in very good agreement with the AGN bolometric luminosity derived from high ionization fine structure lines such as $[\text{O IV}]26\mu\text{m}$. We note that for the data shown in the Figure a linear regression fit gives a slope of 0.9 ± 0.3 for the $[\text{O IV}]$ vs. SED-fit derivations, with the best-fit line crossing the 1-1 relation at $L_{\text{bol}}(\text{SED-fit}) \sim 10^{10} L_\odot$. However, a more accurate analysis should be done on larger and complete samples in order to be used as calibration. On the contrary, X-rays tend to underestimate the AGN luminosity, particularly for highly obscured objects. Indeed, the X-ray bolometric corrections of Compton-thick AGN (empty stars in Fig. 5) derived by Brightman & Nandra (2011) using 2-10 keV X-ray observations increased once hard X-ray measurements became available (e.g., NuSTAR La Caria et al. 2019), moving it closer to the estimation from SED fitting. The possibility that the absorption-corrected 2-10 keV luminosity, and consequently $L_{\text{BOL}}(X)$, is underestimated for moderately obscured/Compton-thick AGN, if additional multi-wavelength data are not taken into account (e.g., SED-fitting), has also been found by Lanzuisi et al. (2015).

Overall, these correlations show the capability of the SED decomposition to derive $L_{\text{bol}}^{\text{AGN}}$ for sources without mid-IR spectroscopy (i.e., too faint or high- z). Once the AGN bolometric luminosity is known, it is possible to compute the black-hole accretion rate, BHAR, (through the standard assumption of 10% efficiency, Hopkins et al. 2007). Similarly, SFRs can be derived from the colder dust component visible in the far-IR (blue curve in Fig. 4) using the standard relations derived for

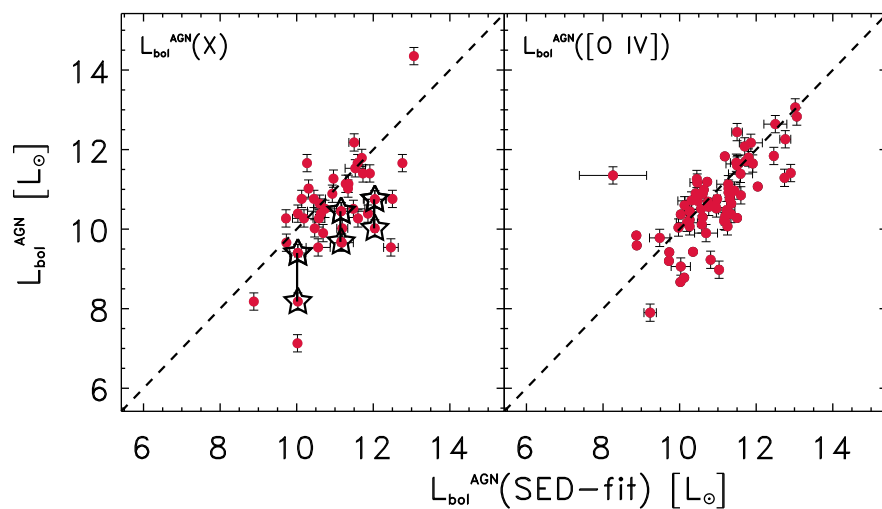


Fig. 5. The power of SED decomposition to derive the AGN bolometric luminosity (L_{bol}^{AGN}), and the BHAR. The panels show the AGN bolometric luminosity derived from SED fitting by Gruppioni et al. (2016) for a local sample of AGN versus the AGN bolometric luminosity derived from different indicators: *left*: X-ray (2–10 keV) Luminosity; *right*: [O IV] 25.9 μm far-IR line. X-ray bolometric correction are taken from Brightman & Nandra (2011). The dashed line represents the 1-1 relation. With PRIMA we will be able to perform similar decompositions at least up to $z = 2$. The stars in the left panel show how the X-ray derived L_{bol}^{AGN} increases for Compton-thick AGN once the hard X-ray spectrum is included (as shown by La Caria et al. 2019). The correlation found in the right panel can be used as a calibration for the SED-fitting results when far-IR spectroscopy is not available.

local galaxies (Kennicutt & Evans 2012) and bright lines such as [Ne II] 13 μm (e.g. Spinoglio et al. 2022).

3. Results

The blending of sources due to the limited spatial resolution of far-IR telescopes can be an important limitation to the ultimate attainable sensitivity in an observation. This limit is usually characterized by a so-called “confusion noise,” which corresponds to the level of the blended background of sources at a given wavelength and resolution. Recent work demonstrates that deblending techniques based on the Bayesian source extractor XID+ can be used to push below the classical confusion (the confusion limit reached by a basic blind source extractor) in PRIMAGER (Donnellan et al. 2024), by leveraging the information provided by shorter wavelengths and the dense wavelength coverage of the instrument. In particular, Donnellan et al. (2024) show that a self-contained approach based on using positional priors from a source catalog detected in the shortest PRIMAGER bands with Wiener-filtering to deblend the longer PRIMAGER wavelengths can reach factors of 2 – 3 below the classical confusion limit. The use of a denser catalog (for example, obtained from *Roman* Space Telescope IR observations of the same field) together with weak intensity priors can push this limit even further, factors of 5 – 10 at the longer wavelengths. Most importantly, Donnellan et al. (2024) show that the self-contained Wiener-filter catalog approach allows PRIMAGER to recover the SEDs of galaxies at the knee of the luminosity function at $z = 2$ out to PPI_2 (see their figures 7 and 9). The calculations presented in the following sections use these results.

3.1. The galaxy population observed by PRIMAGER

As shown in Fig. 6, using the conservative depths we can detect galaxies with $L_{IR} > 10^{13} L_{\odot}$ up to $z = 7 - 8$ in both the deep and wide PRIMAGER surveys. Less-extreme galaxies with luminosities down to $L_{IR} = 10^{11} L_{\odot}$ can be detected to $z = 4$ in the Deep survey and up to $z = 3$ in the Wide survey. As a comparison, with *Herschel* it was possible to observe galaxies with $L_{IR} = 10^{11} L_{\odot}$ only to $z < 1$ (e.g., Gruppioni et al. 2013; Magnelli et al. 2013). If we consider the payload depths, which are the minimal guarantee depths, we lose 28% galaxies in the Deep and 35% in the Wide survey, but in the latter galaxies are limited to $z = 6.5$.

To understand the physical properties of these photometric samples, we present in Fig. 7 the SFR as a function of redshift for both the Deep and the Wide PRIMAGER surveys. Using the conservative depths, we expect the Deep survey to be 50% complete for star-forming galaxies with stellar masses $\log(M_*/M_{\odot}) = 10.5$ and 11.5 up to $z = 2.3$ and $z = 4$, respectively. Note that for galaxies over $\log(M_*/M_{\odot}) = 10.5$ at $z \sim 2$ the study by Donnellan et al. (2024) shows that the SEDs are well measured over a large fraction of the bandpass using the XID+ deblending (see their Figure 9), so we expect to be able to accurately measure their SFR and BHAR. The Wide survey should be 50% complete for galaxies with $\log(M_*/M_{\odot}) = 11.5$ up to $z = 2.9$. Photometric surveys with PRIMAGER would not be limited only to the brightest, most luminous IR galaxies at $z > 1$, as was the case for previous far-IR missions, but would finally start to also include a more representative sample of star-forming galaxies out to cosmic noon and beyond.

3.2. SFR vs. BHAR with PRIMAGER using the far-IR continuum

As previously discussed, the rest-frame continuum between 15 and 150 μm can be used to disentangle the star formation and black hole accretion activity, as the dust heated by these mechanisms has two different temperature distributions. In the next sections we discuss the accuracy of these AGN-SF decomposition using PRIMAGER bands and how we can use these estimates to improve galaxy evolution models.

3.2.1. Parameter Extraction from SEDs

While the mid- and far-IR continuum of galaxies can be used to obtain a simultaneous estimate of both the SFR and the BHAR, the quality of such estimations are correlated with the number of filters used for the SED decomposition and their wavelengths. The PRIMAGER PHI continuous wavelength coverage $\lambda = 25 - 80 \mu\text{m}$ and the PPI filters at $\lambda = 96$ to 235 μm efficiently probe the presence of PAHs for $z \gtrsim 1$ and separate the AGN contribution, peaking at $\lambda_{rest} \sim 20 - 30 \mu\text{m}$, from the emission powered by star-formation, which peaks at $\lambda_{rest} \sim 60 - 120 \mu\text{m}$ (Fig. 4). In this section, we test the ability to recover physical parameters from the SED information provided by PRIMAGER. Specifically, we simultaneously extract the fraction of the total grain mass contributed by PAHs (q_{PAH}), the total IR luminosity

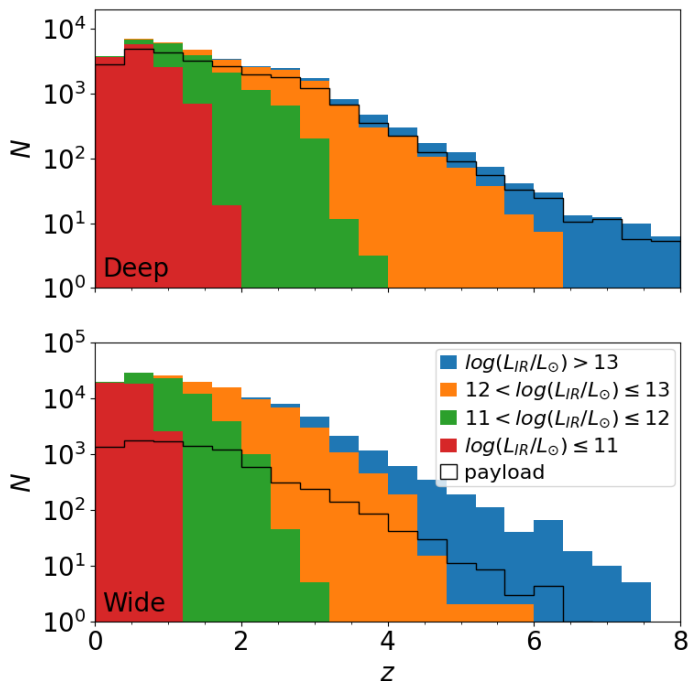


Fig. 6. The proposed PRIMAGER surveys will not be limited to only the brightest IR galaxies. We show the number of galaxies as a function of redshift for the Deep (top, $1500 h/\text{deg}^2$) and Wide (bottom, $150 h/\text{deg}^2$) surveys using the SPRITZ simulation. We considered only galaxies with $S/N \geq 5$ in at least 6 out of 12 PRIMAGER Hyperspectra filters (i.e., PHI1-PHI2 in Table 1). The black solid lines show the total redshift distributions considering the payload depths.

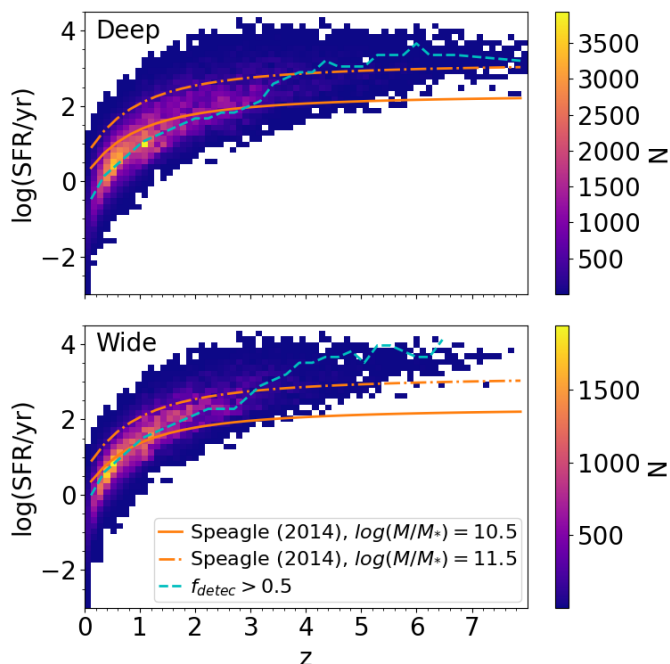


Fig. 7. PRIMA surveys will not be limited to extremely bright objects, but will start to probe normal star-forming galaxies. We show the distribution of SFR as a function of redshift for the Deep (top) and Wide (bottom) surveys, using the conservative depths (see Table 1) and the SPRITZ simulation. The cyan dashed lines indicate the 50% completeness level, while the orange solid and the dash-dotted lines show the SFR of a typical main sequence star-forming galaxy with $\log(M/M_*) = 10.5$ and $\log(M/M_*) = 11.5$, respectively. These have been derived considering the $M_* - \text{SFR}$ relation by Speagle et al. (2014) at different redshifts.

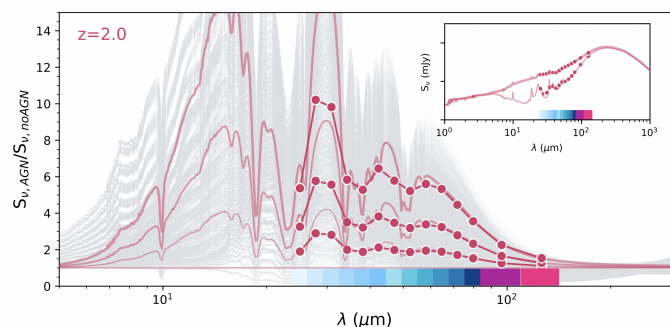


Fig. 8. Contribution of AGN emission into the PRIMAGER bandpass, showing that the PRIMAGER bands are very sensitive to the presence of an AGN. Thin grey lines show a $z = 2$ galaxy SED including different AGN properties (see Table 2), divided by the SED without an AGN component. As an example, the emission of one AGN model with different f_{AGN} contributions (15, 30, and 45% of the total IR luminosity) is shown in red thick lines. The fluxes obtained for integration in the equivalent filters with center wavelengths listed in Table 1 for PHI+PPI1+PPI2 are shown as red circles. The inset panel shows the SEDs corresponding to the red lines (for $f_{\text{AGN}} = 0\%$ and $f_{\text{AGN}} = 45\%$) over the full UV to submm wavelength range. The PRIMAGER bands are well suited to probe the impact of AGN emission on the IR SED of galaxies.

(L_{IR}), and the fraction of the total IR luminosity due to an AGN (f_{AGN}) using SED modeling.

We use CIGALE³ (Boquien et al. 2019) to compute multi-wavelength SEDs of AGN host galaxies (Ciesla et al. 2015; Yang et al. 2020, 2022). This analysis is performed in a self-consistent way (i.e. creating and analysis the models with the same tool) and over a grid of SED templates wider than the one included in SPRITZ, to avoid introducing any systematic uncertainties due to the SED fitting procedure or the simulation. In particular, the *skirtor* library (Stalewski et al. 2016) is used to model the AGN emission. Dust emission is modelled with the library of Draine et al. (2014), an extended version of the models of Draine et al. (2007). We create a set of AGN+host galaxy SEDs at different redshifts (our mock catalogue), varying dust emission and AGN properties (see Table 2), including the contribution of the AGN to the total L_{IR} (f_{AGN}) to create a wide range of SED types. The SEDs are built with q_{PAH} values varying from 0.47% to 7.32% to probe a wide range of SEDs. Schreiber et al. (2018) showed that q_{PAH} can vary from approximately 7% down to 2.5% between $z = 0$ and $z = 3$. Furthermore, in the local universe, typical normal star-forming galaxies have a q_{PAH} ranging from 1.22 to 4.58% (Ciesla et al. 2014). Therefore, the dynamical range of q_{PAH} probed in this test covers typical values found in the literature. Regarding the AGN contribution, we use f_{AGN} ranging from 0. to 0.5 which is consistent with the range of AGN fractions measured by Małek et al. (2018) when fitting *Herschel* IR galaxies. For reference, the range of f_{AGN} explored here corresponds to a range of $f_{\text{AGN},\text{MIR}}$ from 0–90% (Kirkpatrick et al. 2015).

In Figure 8 we show the variety of these mock SEDs and how the AGN contribution is well probed by the wavelengths covered by PRIMAGER, using as example an object at $z = 2$. The faint grey lines show the SED of our mock galaxies divided by that of a galaxy of the same luminosity without an AGN component, highlighting the fact that the effect of an AGN is significant at the wavelengths probed by the PHI.

³ <https://cigale.lam.fr/>

Table 2. Parameters of the models used to build the mock SEDs with CIGALE.

Parameter	Value	
Dust emission: (Draine et al. 2014)		
q_{PAH}	0.47, 1.12, 1.77, 2.50, 3.19, 3.90, 4.58, 5.26, 5.95, 6.63, 7.32	Mass fraction of PAH
α	2.5	Slope $dU/dM \propto U^\alpha$
γ	0.001, 0.02, 0.2	Fraction illuminated from min. to max. radiation field
U_{min}	2, 10, 20, 30	Minimum radiation field
AGN emission: SKIRTOR (Stalevski et al. 2016)		
t	3, 5, 7	Opt. depth at $9.7\mu\text{m}$
i	30, 60	Viewing angle
f_{AGN}	[0;0.5] by steps of 0.05	Contribution of the AGN to the total L_{IR}
z	1, 2	Redshift

We associate flux errors to the modelled fluxes, considering both the contribution from the instrumental (Table 1) and the confusion noise. We use the PHI1_4 filter ($\lambda = 34\mu\text{m}$) as the detection band, because observations at that wavelength will not suffer from confusion (B  thermin et al. 2024), and compute the fluxes in the remaining filters from their ratio to PHI1_4, while maintaining the overall SED shape. Classical confusion noise is usually derived for a blind detection strategy at a single wavelength, but PRIMAGER’s broad and dense wavelength coverage enables more refined strategies that overcome such limitations. Donnellan et al. (2024) show that a self-contained Bayesian deblending approach implemented using XID+ (Hurley et al. 2017) reaches flux densities a factor of $\sim 2 - 3$ fainter than the classical confusion limit estimated in B  thermin et al. (2024). We thus take the confusion noise values found by Donnellan et al. (2024) using their Wiener-filter derived catalogue, add them in quadrature to the instrumental noise to determine the total noise, and require a S/R of 10 in the PHI1_4 filter for our recovery experiment. We also compute the results requiring S/R=5 in PHI1_4, which show a mild degradation and are in general intermediate between the extraction with PPI1+PPI2 and just PPI1 alone. We also show the result of a run using S/R=10 and the lower confusion noise obtained in XID+ extractions when using a deep catalog with some prior intensity information (Donnellan et al. 2024).

To test the quality of the parameter extraction we fit the mock catalogue for q_{PAH} , f_{AGN} , and L_{IR} simultaneously, using the Bayesian-like analysis performed in CIGALE. We first do a run including data from PHI, then a run using PHI+PPI1, and a final run using PHI+PPI1+PPI2. In Fig. 9, we show the distribution of the difference between the physical properties estimated through this process and their true value, considering galaxies with redshifts of 1 and 2. Broadly speaking the histograms show very little or no bias for q_{PAH} and f_{AGN} , while there is a mild bias in L_{IR} when the PPI filters are not included. As expected, the histograms also tighten up when more wavelength information is included, and they show little to no degradation if the S/R is dropped from 10 to 5 at our anchoring filter PHI_4.

Quantitatively, the histograms show a number of trends. Because the PAH emission is weakened or erased from the SED in the presence of a strong AGN continuum, we test the recovering of q_{PAH} in cases where there is no AGN contribution. The

impact of reducing the wavelength coverage is on the width of the distribution, going from a dispersion of 0.9 with the full PHI plus two first filters of PPI to a flatter distribution when only using PHI (dispersion of 1.3). The AGN fractional contribution to the total L_{IR} (f_{AGN}) is well recovered when the full PHI band and the two first PPI filters are used: the distribution is centred on zero and has a dispersion of 0.06. The bias introduced by removing the PPI filters is very slight, just 0.02, and the dispersion increases by 30% to 0.08. Finally, the distribution of the difference between the estimated L_{IR} and its true value, in logarithmic scale, is centred on zero and has a dispersion 0.1 dex when all filters are included, but the median is biased high to +0.05 with a dispersion of 0.15 dex when we rely on PHI only.

It is also interesting to look at how the extraction results for f_{AGN} and L_{IR} vary as a function of both q_{PAH} and f_{AGN} . We show the systematic error and dispersion in our extraction in Fig 10 computed for $z = 1$ and $z = 2$, when employing a filter set that includes the full PHI, and PPI1 + PPI2. The dispersion of the $f_{AGN} - f_{AGN,true}$ distribution is on average 0.05, and below 0.12 over most of the parameter space. The highest uncertainty is found at $z = 2$ for very low intrinsic PAH abundance, $q_{PAH} < 2\%$, and intermediate AGN contributions, $0.15 < f_{AGN} < 0.35$. These tests show that the PRIMAGER bands are well-suited to probe the AGN emission and disentangle it from the emission due to star-formation for a vast range of source properties. The bottom row of Fig. 10 shows that the L_{IR} is very well recovered at $z = 1$ with a dispersion on the $\log L_{IR} - \log L_{IR,true}$ distribution well below 0.12 dex for all the parameter space explored. At $z = 2$ the filters probe shorter rest-frame wavelengths, further away from the peak in the far-IR, but the combined use of the PHI and the two first filters of PPI still allows for good recovery of the L_{IR} with an average dispersion of 0.1 dex and a maximum of 0.25 dex.

To understand the impact of the longest wavelength SED points on the accuracy of the extracted parameters, we show in Fig. 11 the median value of the distributions shown in Fig. 9 and Fig. 10 for f_{AGN} and L_{IR} at $z = 2$, after removing one or both PPI filters. When removing the PPI2 filter (left column), f_{AGN} is still well recovered with a bias that is lower than 0.05 in half of the parameter space tested here, except in the region of weak PAH and intermediate AGN contribution where it can reach up to 0.15, while for the L_{IR} the bias can reach up to 0.25 dex. If only the full PHI band is used (right column), biases for both f_{AGN} and L_{IR} also reach up to 0.15 and 0.25 dex, respectively, but on a wider proportion of the parameter space. Therefore we conclude that the inclusion of the PPI fluxes are necessary to derive accurate PAH, SFR and AGN parameters, particularly for sources at $z = 2$ where the PHI band probes only up to $27\mu\text{m}$ rest-frame wavelengths.

3.2.2. Expected Distributions

State-of-the-art galaxy evolution models show order of magnitude disagreements in their predictions of the distribution of the ratio of BHAR/SFR (Habouzit et al. 2020, 2021). In general, models calibrated on physical quantities derived from UV/optical/near-IR data (for example, stellar mass, SFR) such as IllustrisTNG and the SC SAM (Somerville et al. 2008, 2015) predict faster black hole growth at high masses and luminosities, with the consequent quenching of the star formation activity. Empirical models calibrated on far-IR data from the *Herschel* telescope such as SPRITZ or the Simulated Infrared Dusty Extragalactic Sky (SIDES, B  thermin et al. 2017), on the other hand, predict slower black-hole growth and more vigorous dust-

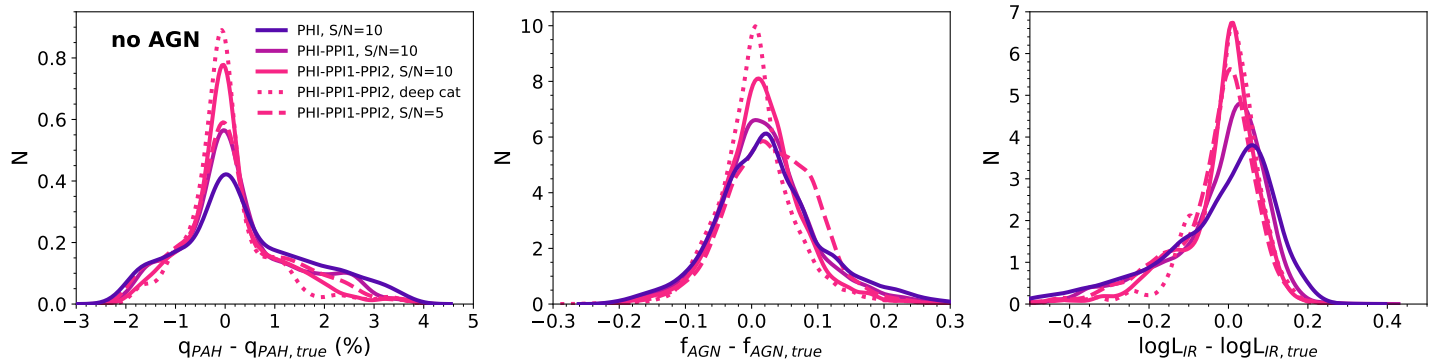


Fig. 9. Normalised distributions of the difference between the estimated and the true values of the extracted parameters. In each panel, the lines are colour-coded according to the set of filters used in the fitting. The distributions include all models whose parameters are described in Table 2. The same distributions, with the PHI+PPI1+PPI2 set of filters but assuming a S/N of 5 instead of 10 in PHI₁₋₄ are shown in dashed line. The dotted line shows the results using the confusion noise for the deep catalog from Donnellan et al. (2024), attainable in regions where ancillary information exists (e.g., from the *Roman* Space Telescope). Left panel: PAH fraction measured in percent (q_{PAH}). Centre panel: AGN fractional contribution to the total IR luminosity (f_{AGN}). Right panel: total IR luminosity ($\log L_{IR}$). The distributions do not show any bias for the estimate of the PAH fraction and the AGN fraction at $z = 1$ and $z = 2$. The $\log L_{IR}$ estimated with only the PHI presents a bias of +0.07 dex and a tail toward larger underestimates (factors of 2 to 3). Dropping the required S/R from 10 to 5 in the PHI₁₋₄ has only a very modest impact in q_{PAH} and f_{AGN} and does not introduce any biases.

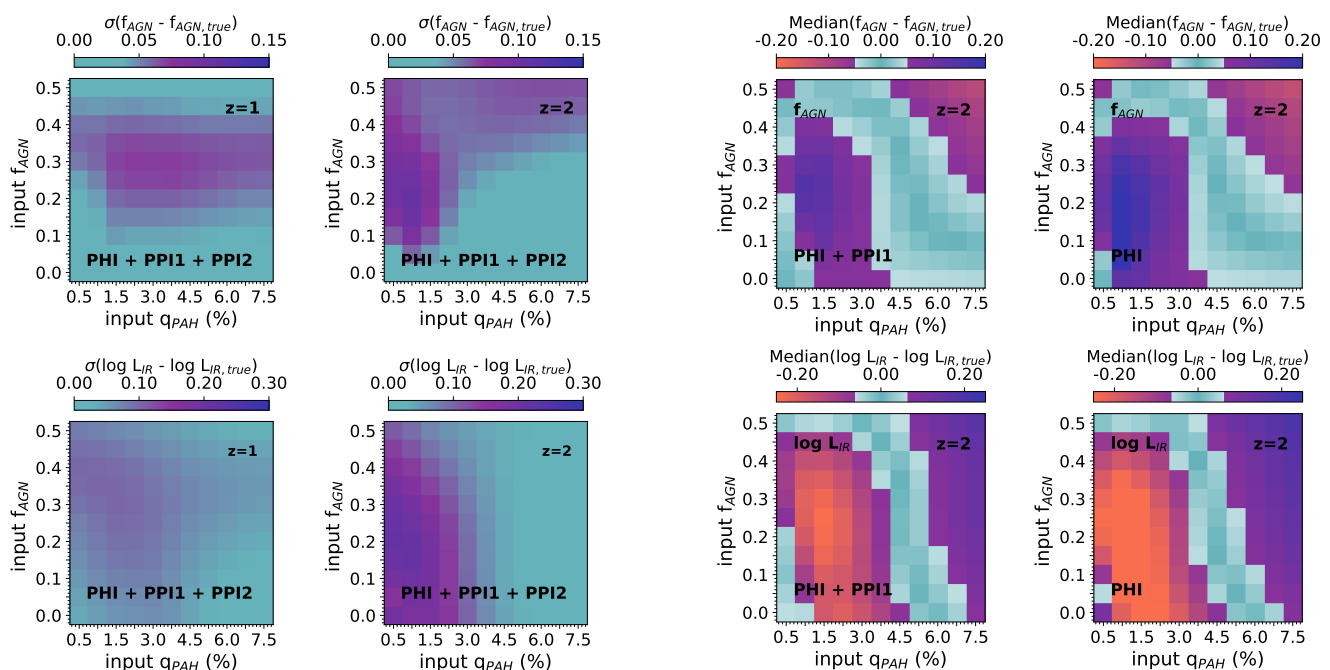


Fig. 10. Extraction of f_{AGN} and L_{IR} as a function of AGN contribution and PAH fraction. The AGN fraction is well recovered over all the parameter range probed by the test, with an error < 0.1 at both $z = 1$ and $z = 2$. The IR luminosity is recovered to better than 0.12 dex, at $z = 1$ and with a dispersion lower than < 0.25 dex at $z = 2$. Top row panels: panels are colour-coded according to the standard deviation of the $f_{AGN} - f_{AGN,true}$ distribution. Left panel and right panels present the results at $z = 1$ and $z = 2$, respectively. Bottom row panels: same as top row panels for the L_{IR} .

enshrouded star formation in luminous systems. The main reason for this discrepancy is that much of the stellar and black hole growth takes place behind large screens of gas and dust that absorbs photons from the near-IR to the soft X-ray bands (Hickox & Alexander 2018).

Figure 12 shows a comparison of the $z = 1 - 1.5$ slice of a survey of a galaxy population synthesised using SPRITZ, with that

Fig. 11. Impact on parameter extraction accuracy of removing long wavelength information at $z = 2$. The inclusion of the longer wavelengths improves the accuracy of the determinations, but the degradation is fairly smooth. Top row: median value of $f_{AGN} - f_{AGN,true}$ as a function of f_{AGN} and L_{IR} . Bottom row: same but for $\log L_{IR} - \log L_{IR,true}$. The left side and right side panels use the PHI band plus PPI1 and only in the full PHI band, respectively, to extract the parameters.

synthesised using the SC SAM over the same 10 square degree light-cone (Yung et al. 2022). These calculations use the depth attainable with the conservative performance of PRIMAGER in 150 hours per square degree (i.e., Wide survey in Tab. 1), and the extraction depth attainable using a source extraction based on the software XID+ (Donnellan et al. 2024) requiring that the sources are detected at 5σ or better over half the bandpass of PHI. The key difference is that SPRITZ predicts a much larger number of composite AGN-starburst systems, as well as many

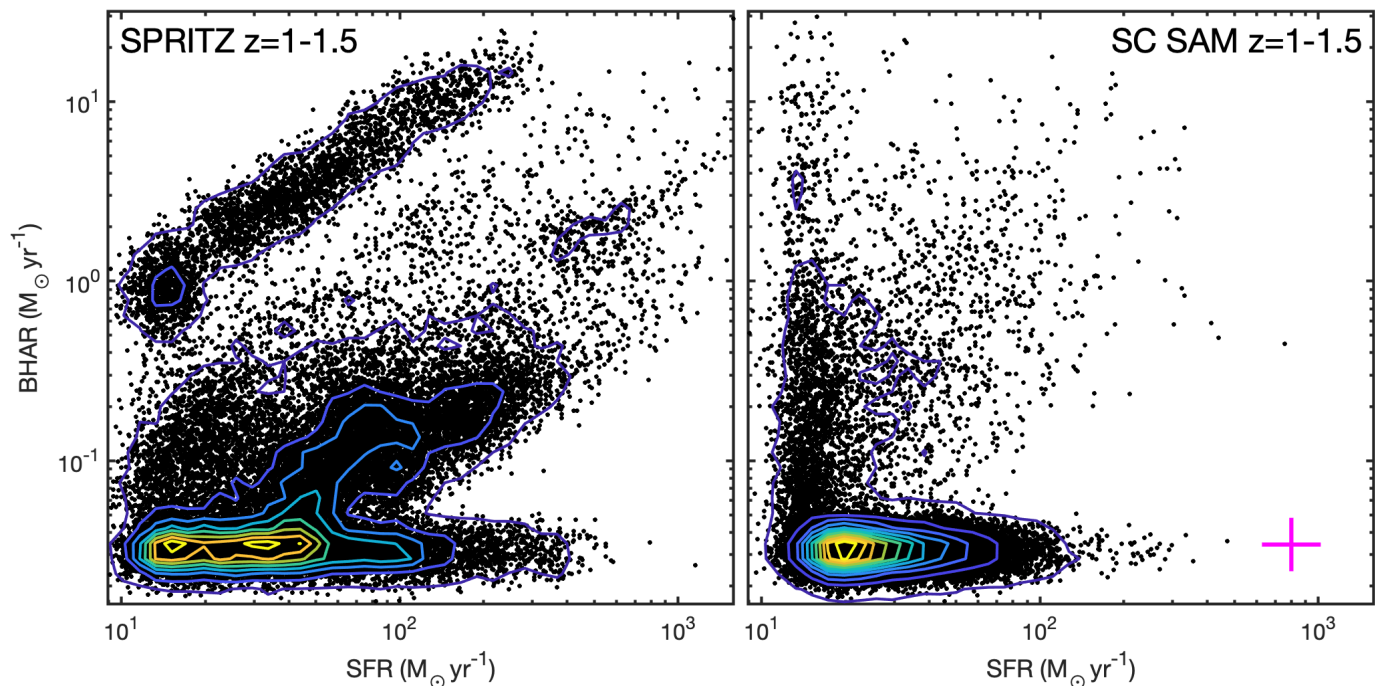


Fig. 12. Comparison of expected galaxy distributions in SFR and BHAR from SPRITZ and the Santa Cruz SAM over a 10 sq. deg. light-cone with an integration time of ~ 150 hrs. per square degree. The contours indicate density of sources, and the magenta cross in the right panel shows the expected extraction uncertainties for the median galaxy (§2.4). Each panel has about 30,000 sources detected at 5σ or better over half the PHI bandpass, but only $\sim 4\%$ are hybrid AGN+SF galaxies in the SC SAM, while $\sim 44\%$ of the SPRITZ sources are hybrid. In models like the SC SAM the rapid growth of the black hole leads to stopping the star formation activity, while empirical models calibrated against far-IR data like SPRITZ predict a large number of co-evolving systems.

more galaxies with larger SFRs than the SC SAM. In the SC SAM, only $\sim 4\%$ of the galaxies have $\text{BHAR} > 0.06 M_{\odot} \text{yr}^{-1}$ and $\text{SFR} > 20 M_{\odot} \text{yr}^{-1}$, while for SPRITZ that fraction is $\sim 44\%$. The fairly large discrepancy between models highlights the urgent need for deep surveys with a sensitive, far-IR telescope like PRIMA that can disentangle star formation and AGN powered emission within large numbers of dusty galaxies at cosmic noon. The fast mapping capabilities of PRIMAgger will enable sample sizes detected with PRIMAgger that are $100\times$ to $1,000\times$ larger than those available from *Herschel* (Magnelli et al. 2013; Delvecchio et al. 2014), providing us with a true statistical view of black hole and star formation activity during the formative era of galaxies.

3.3. SFR vs. BHAR with FIRESS using far-IR lines

As already mentioned, using far-IR spectroscopy it is possible to have a direct estimate of both the BHAR and the SFR for the same object. Indeed, the $[\text{O IV}]26\mu\text{m}$ line is a robust calibration of the BHAR, while the $[\text{Ne II}]13\mu\text{m}$ line is an accurate indicator of the SFR (e.g., Spinoglio et al. 2015; Stone et al. 2022). In the case of the $[\text{O IV}]26\mu\text{m}$ line, the contribution excited by star formation can be accounted for (Stone et al. 2022), and the blended contribution from the much fainter nearby $[\text{Fe II}]26\mu\text{m}$ line will not affect the measurement. In Fig. 13 we show how the predicted flux of these two lines change with the IR luminosity, the AGN fraction (defined between 8 and $1000 \mu\text{m}$) and the redshift, as derived from SPRITZ.

We concentrate on fluxes down to $10^{-19} \text{W}/\text{m}^2$, which is feasible for point sources with FIRESS in the low-resolution mode ($R \sim 100$) with one hour of integration time. We however highlight that this depth is just chose as an example and it

is indeed possible to integrate more time with FIRESS. In details, observations down to $10^{-19} \text{W}/\text{m}^2$ allows for tracing the $[\text{Ne II}]13\mu\text{m}$ line in galaxies of $L_{\text{IR}} = 10^{11} L_{\odot}$ up to $z = 0.7$, while galaxies of $L_{\text{IR}} = 10^{12.5} L_{\odot}$ can be observed up to $z = 3$. These fluxes show little dependence on the AGN fraction, given that $[\text{Ne II}]13\mu\text{m}$ line mainly traces star-formation. The $[\text{O IV}]26\mu\text{m}$ line, which efficiently traces AGN activity, is instead generally fainter than the $[\text{Ne II}]13\mu\text{m}$ line, therefore similar observations trace galaxies of $L_{\text{IR}} = 10^{11.0} L_{\odot}$ up to $z = 0.4$ for $f_{\text{AGN}} < 0.5$, but up to $z = 0.8$ for higher AGN fractions. At the same time, the $[\text{O IV}]26\mu\text{m}$ line is brighter than $10^{-19} \text{W}/\text{m}^2$ in galaxies of $L_{\text{IR}} = 10^{12.5} L_{\odot}$ up to $z = 1$, if $f_{\text{AGN}} < 0.5$, and up to $z = 1.8$ for higher AGN fractions. To put these values in a broader context, we also report the line fluxes for galaxies at the knee of the IR luminosity function, as derived by Traina et al. (2024), and six times above it. The galaxies with $[\text{O IV}]26\mu\text{m}$ or $[\text{Ne II}]13\mu\text{m}$ line brighter than $10^{-19} \text{W}/\text{m}^2$ are generally beyond the knee of the luminosity function, but are not tracing hyper-luminous IR galaxies ($L_{\text{IR}} > 10^{13} L_{\odot}$). Moreover, it is necessary to take into account that there will be several other low-ionisation far-IR fine-structure lines that trace star formation or AGN. Correlating these lines could potentially enable us to detect galaxies to greater depth and to give confidence in weaker line detections.

In order to simultaneously derive SFR and BHAR to trace possible signatures of co-evolution between the AGN and its host galaxy, it is necessary to observe both $[\text{O IV}]26\mu\text{m}$ and $[\text{Ne II}]13\mu\text{m}$ in the same galaxies. This will be possible only for a subsample of the aforementioned objects, whose redshift distribution is shown in Fig. 14. This subsample corresponds to around 19,000 objects/deg 2 up to $z = 5.5$, of which $\sim 15,800$ objects/deg 2 are at $z > 0.8$ and inside the FIRESS wavelength coverage. Among the latter, 91% and 59% of the galaxies are

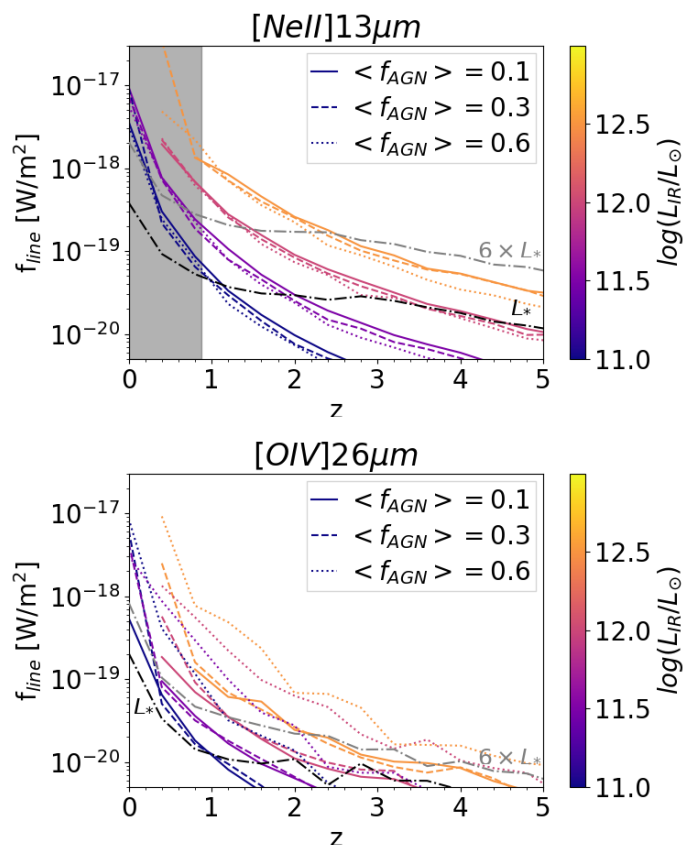


Fig. 13. Spectroscopic follow-up of galaxies down to 10^{-19} W/m^2 will start probing more normal galaxies and not only ultra-luminous IR galaxies. We show the $[\text{Ne II}]13\mu\text{m}$ (top) and $[\text{O IV}]26\mu\text{m}$ (bottom) line fluxes as a function of redshift, total IR luminosity (see color bar) and IR AGN fraction (different line styles in bins with $\Delta f_{\text{AGN}} = 0.2$). Dashed dotted lines indicate the line fluxes for galaxies in the knee of the IR luminosity function and six times above it (Traina et al. 2024). The grey area on the top panel shows the redshift range in which the $[\text{Ne II}]13\mu\text{m}$ line is not in the PRIMA/FIRESS wavelength coverage.

expected to be also detected with PRIMAgger above the Deep and Wide depths, respectively. In particular, the deep photometric survey includes $> 90\%$ and $> 50\%$ of objects with $[\text{O IV}]26\mu\text{m}$ and $[\text{Ne II}]13\mu\text{m}$ up to $z = 2$ and $z = 3.6$. Therefore, the Deep PRIMAgger photometric survey can efficiently be used to select target to follow-up in spectroscopy to validate and calibrate the SFR and BHAR derived through the SED-fitting analysis.

3.4. The PAH metallicity dependence

Up to 20% of the total infrared emission in galaxies emerges as vibrational emission at $3\text{--}18\mu\text{m}$ of small carbon-rich PAH grains (Smith et al. 2007). *Spitzer* observations of PAHs in the local Universe uncovered a strong dependency of the strength of PAH emission on the gas phase metallicity, with an apparent steep decline in the PAH abundance at metallicities of less than $\sim 25\%$ solar (Engelbracht et al. 2005; Smith et al. 2007; Draine et al. 2007; Hunter et al. 2010; Sandstrom et al. 2012; Aniano et al. 2020; Whitcomb et al. 2023). This connection between small grain emission and gas metal abundance ties directly to the lifecycle of PAHs, with indications from changing size and heating-sensitive band ratios of strong evolution in the distribution of grain sizes and potential photo-destruction in high intensity, UV-bright radiation environments. As explored by Calzetti et al. (e.g.

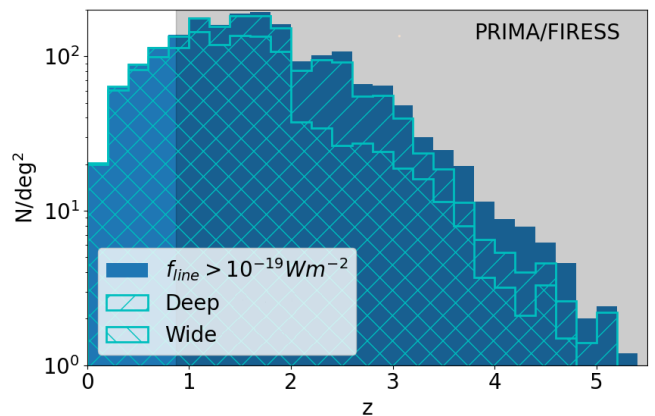


Fig. 14. The photometric survey can be used to identify galaxies to follow-up in spectroscopy. We show the redshift distribution of galaxies with $[\text{O IV}]26\mu\text{m}$ and $[\text{Ne II}]13\mu\text{m}$ lines above 10^{-19} W/m^2 (blue histogram) with the subsamples detected in the Deep and Wide surveys (hatched histograms), considering the conservative depths. The grey area shows the redshift range in which $[\text{O IV}]26\mu\text{m}$ and $[\text{Ne II}]13\mu\text{m}$ lines are in the PRIMA/FIRESS wavelength coverage, but other lines can be used at $z < 0.8$ to derive SFR and BHAR.

2007), the metallicity-dependence of PAH emission also impacts their use and calibration as indicators of SFR and AGN fraction.

JWST is now uncovering evidence that PAHs are deficient in lower mass (and likely lower metallicity) galaxies approaching cosmic noon (Shivaei et al. 2024), and has also identified unexpectedly strong UV absorption in the 2100\AA feature sometimes attributed to PAHs at redshifts as high as $z = 7$ (Witstok et al. 2023). JWST spectroscopic mapping observation of a strongly-lensed dusty luminous galaxy at $z = 4.1$ revealed strongly varying PAH $3.3\mu\text{m}$ emission (Spilker et al. 2023), in what is currently the earliest known PAH detection. Yet the majority of PAH power shifts out of JWST's passbands by $z = 2.1$, and the long-wavelength spectroscopic sensitivity of JWST Mid-Infrared Instrument limits the study of PAH emission to the single $3.3\mu\text{m}$ band which comprises just a few percent of the total PAH luminosity (Lai et al. 2020). At cosmic noon and earlier times, the bulk of PAH power shifts into PRIMA's far-IR passbands (see Fig. 1).

SPRITZ predicts that samples of the order of $\sim 10^4$ PAH-emitting galaxies will be detected in the deep hyper-spectral survey (Fig. 6), including luminous sources out to $z = 8$. At $z \sim 2$, the metallicity measure based on $[\text{N III}]57\mu\text{m}$, $[\text{O III}]52\mu\text{m}$ and $[\text{O III}]88\mu\text{m}$ lines (N3O3 method, Sect. 2.2) combines with direct hyper-spectral and spectroscopic recovery of PAH luminosity to directly test models of PAH lifecycle and metal sensitivity during the epoch when dust and metal production peaked in the Universe. As visible in Fig. 15, we expect $850 \text{ objects/deg}^2$ to have all the three lines necessary for the N3O3 measure (i.e. $[\text{N III}]57\mu\text{m}$, $[\text{O III}]52\mu\text{m}$, $[\text{O III}]88\mu\text{m}$) above 10^{-19} W/m^2 at $z < 1.7$, which is the maximum redshift at which FIRESS can observe $[\text{O III}]88\mu\text{m}$. Almost all ($> 98\%$) these galaxies are expected to be detected in the PRIMAgger surveys. At $z = 1.5\text{--}2.5$, we instead expect to observe around $2,000 \text{ objects/deg}^2$ with both $[\text{N III}]57\mu\text{m}$ and $[\text{O III}]52\mu\text{m}$ lines above the same flux limit. Moreover, considering the conservative depths, 72% and 43% of these objects will be detected in the PRIMAgger Deep and Wide surveys, respectively. These fractions change by 1% or less if we consider the payload sensitivities. This shows that the Deep photo-

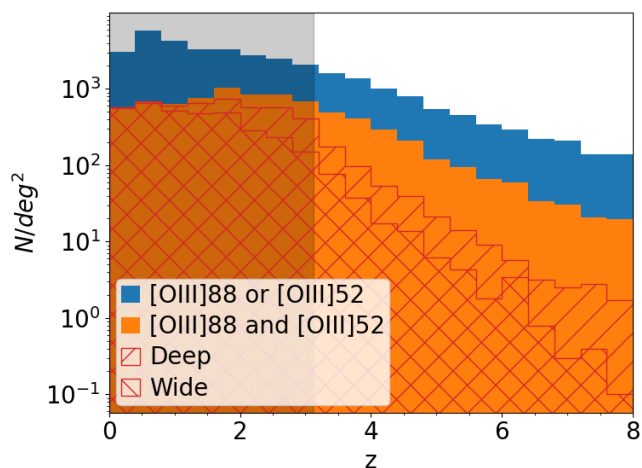


Fig. 15. Redshift distribution predicted in *SPRITZ* for galaxies with $[\text{N III}]57\mu\text{m}$, $[\text{O III}]52\mu\text{m}$ and/or $[\text{O III}]88\mu\text{m}$ lines above 10^{-19} W/m^2 . The hatched histogram shows the sub-population that is also detected in the Deep and Wide PRIMAger surveys, considering the conservative depths. The grey area shows the redshift range in which $[\text{N III}]57\mu\text{m}$ and $[\text{O III}]52\mu\text{m}$ lines are in the PRIMA/FIRESS wavelength coverage.

metric survey can be used as prior to select objects to follow-up with FIRESS.

3.5. Predicting and Observing Galactic Outflows

Galactic outflows, whether driven by AGN or the collective effects of supernovae, are believed to play an important role in galaxy evolution. These outflows can heat or even remove entirely the gas available for future star formation as well as reduce or halt gas infall from the CGM. Outflows are known to be very common in luminous and ultraluminous IR galaxies in the local universe (e.g., Veilleux et al. 2013), with velocities that can exceed 1000 km s^{-1} . They are invariably multi-phase, with a cool component thought to dominate the mass and momentum of the outflow. This cool component can be observed and characterised directly in the far-IR, most commonly via far-IR OH lines observed in absorption against the far-IR continuum of the host galaxy (Spoon et al. 2013; Veilleux et al. 2013; Stone et al. 2016). In particular, mass outflow rates can be derived using OH rotational doublets at 65, 71, 79, and $84 \mu\text{m}$ and used in conjunction with radiative-transfer models to estimate the physical parameters of the cool component of the wind, most importantly the mass and mass outflow rates, which can match and in some cases exceed the SFRs even in the most luminous galaxies (González-Alfonso et al. 2017).

To predict the occurrence of outflows and estimate their properties over cosmic time we need to rely on simulations. Hydro-dynamical simulations, in particular, can be used to model the properties and effects of outflows in individual and ensembles of galaxies, but the detailed physics and implementation varies significantly (Wright et al. 2024). Just as importantly, these simulations are extremely costly to run, and it is infeasible to simulate the large volumes that will be surveyed by future telescopes like PRIMA. All simulations predict strong outflows associated with rapidly growing galaxies and supermassive black holes, although the details vary from simulation to simulation. To estimate the galactic outflows that we can expect to study with PRIMA, we use scaling relations extracted

from one such simulation and “paint” them on top of the galaxy population in the *SPRITZ* model. In order to do this, we make use of the galactic outflows in IllustrisTNG Wright et al. (2024), and statistically relate them to galaxy properties as available in both IllustrisTNG and *SPRITZ*. We start by converting the BHARs and SFRs to galaxy bolometric luminosities using the standard recipes (assuming an efficiency of 10% for the accretion, and using the Kennicutt & Evans 2012, conversion between SFR and luminosity). We then derive a relation between bolometric luminosity and outflow mass loss rate (\dot{M}_{out}), as measured at a scale of $0.1 r_{\text{vir}}$ from the centre of the galaxy halo at redshift $z = 2$, where r_{vir} is the halo virial radius.

These results in a correlation between the mass outflow rate (in $M_{\odot} \text{ yr}^{-1}$) and the bolometric luminosity (in L_{\odot}), such that $\log(\dot{M}_{\text{out}}) = 0.54 \log(L_{\text{bol}}) - 4.13$, with a tail of objects that scatter toward higher mass-loss rates (Figure 16). The relative importance of the tail is larger when considering systems with higher outflow velocities, containing just over 2% of the systems with outflows at $0.1 r_{\text{vir}}$ to just over 7% for systems with outflow velocities $\geq 250 \text{ km s}^{-1}$ at $0.1 r_{\text{vir}}$. Note that a system being in the high-velocity tail of the distribution does not correlate with it harbouring an energetically important AGN at the time of the measurement (red symbols in Figure 16), and may instead reflect past AGN activity.

Figure 17 shows the result of applying the relation described above to the *SPRITZ* simulations of the infrared sky. Since the models are sparsely populated at the high luminosity end, an assumption here is that the derived relation can be extrapolated to galaxies with very large bolometric luminosities (approaching or even exceeding $10^{13} L_{\odot}$). This is reasonable since these luminous systems represent dusty galaxies where the stellar mass and/or the central black hole are accreting and growing at their largest rates, and these also are expected to host the most powerful outflows - just as they do at low redshift when they are much more rare. In Figure 17 we show the density of systems that would be well detected (those detected at 5σ or larger over more than 50% of the PRIMAger Hyper-spectral Imager logarithmic pass-band) in a PRIMAger survey with 150 hours of integration per square degree, at the conservative performance expected for the instrument. Scaling results obtained for the outflow in the nearby ULIRG Mrk 231 (González-Alfonso et al. 2014), we estimate that it is possible to use FIRESS operating at $R \approx 900$ to detect and characterize these winds via the $84\mu\text{m}$ OH line for over 200 luminous IR galaxies detected with PRIMAger at $z \sim 1 - 2$ (those brighter than 120 mJy at $210 \mu\text{m}$). This will expand, by more than an order of magnitude, the number of sources with powerful, massive outflows studied spectroscopically in the far-IR, and allow us to probe quenching in dusty galaxies at cosmic noon, and the subsequent decline in star formation, for the first time.

4. Summary and conclusions

The most active phases of star-formation and black-hole accretion in galaxies are hidden behind large columns of gas and dust. Studying critical phases in the co-evolution of super-massive black holes and galaxies therefore requires the ability to penetrate the resulting extinction, and bring to bear sensitive diagnostic tools to study the physical conditions in distant galaxies. The mid and far-IR part of the spectrum provides abundant well-understood diagnostics of the atomic and molecular gas, as well as the dust, providing a window into star formation, black hole growth, metallicity, and feedback driven galactic outflows in even the most obscured galaxies. In this work, we have

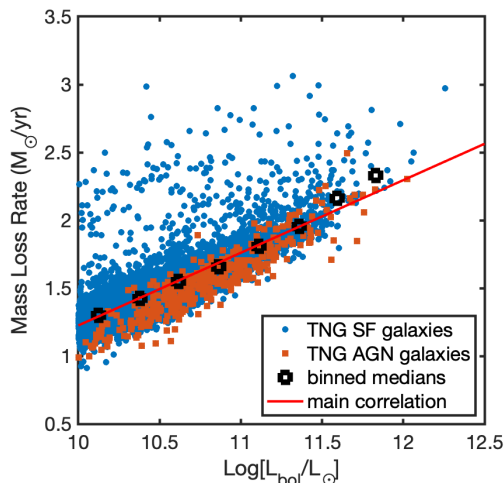


Fig. 16. Correlation between bolometric luminosity and outflow mass-loss rate in IllustrisTNG simulations. Red square symbols represent galaxies where L_{bol} has a $\geq 20\%$ contribution for the AGN, while blue symbols are all other galaxies. The median mass-loss rate in bins of L_{bol} is shown by the black symbols. The main correlation, $\log(\dot{M}_{\text{outf}}) = 0.54 \log(L_{\text{bol}}) - 4.13$, is shown by the red line.

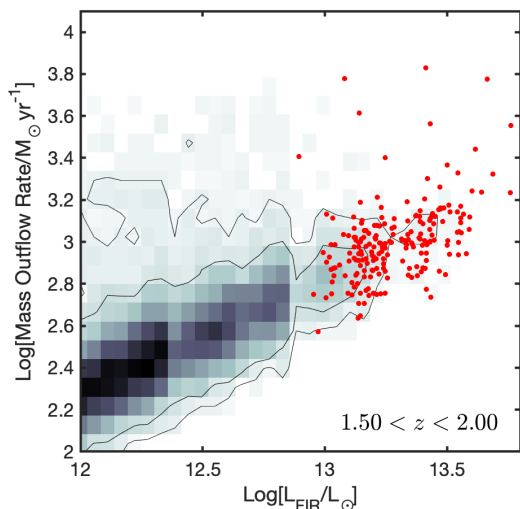


Fig. 17. Predicted mass-loss rates in SPRTZ galaxies well-detected with PRIMAGER in a 10 sq. deg. survey with 150 hours of integration per square degree, for the redshift range $1.5 < z < 2$, using an extrapolation of the relation described in §3.5. The red galaxies (about 200 of them) are brighter than 120 mJy at $210 \mu\text{m}$, and thus can be followed up in velocity-resolved OH absorption spectroscopy in a moderate integration. These are very rapidly growing systems, expected to host massive winds.

demonstrated the photometric and spectroscopic capabilities of the PRIMAGER mission to address key questions in our understanding of how galaxies and super-massive black holes evolve together over a significant fraction of cosmic time.

In particular, we have shown that multi-tiered photometric surveys conducted with PRIMAGER will allow us to detect and study galaxies hundreds of times fainter than were reachable by previous far-IR observatories (e.g. *Herschel*, *Spitzer*), reaching the bulk of the population to cosmic noon and beyond. PRIMAGER will be able to observe normal ($10^{11} L_{\odot}$), star-forming galaxies up to $z = 4$, and its dense wavelength coverage efficiently probes the presence of PAHs for $z \gtrsim 1$ and can also

be used to accurately separate AGN and star-formation heating by measuring the shape of the IR dust continuum. Using simulations based on the deepest existing far-IR surveys, along with semi-analytic models of evolving galaxies and dark matter halos, we have made predictions of the galaxy populations that could be observed with PRIMAGER and FIRESS, along with quantitative estimates of the accuracies with which we can disentangle and measure the signatures of star formation, black hole growth, gas-phase metallicity, and galactic outflows as a function of IR luminosity, redshift and survey area. In particular, we have verified that, using SED-decomposition we are able to retrieve the AGN fraction with respect to the total IR luminosity with a dispersion of 0.06, the fraction of dust mass contributed by PAH (q_{PAH} , measured in percentage) with a dispersion of 0.9, and the total IR luminosity with a scatter of 0.1 dex (§2.4). Because of its ability to map large areas of the sky to great depths, PRIMAGER can be used to generate and measure large samples of dusty galaxies which are $100\times$ to $1,000\times$ larger than those available from *Herschel* (Magnelli et al. 2013; Delvecchio et al. 2014) out to the epoch of peak star formation and black hole growth.

Spectroscopic follow up with the FIRESS instrument on PRIMAGER will reach unprecedented depths in the far-IR, 10^{-19}W/m^2 in one hour of integration at $R = 100$, allowing detection of faint fine structure lines and PAH emission features which can be used to directly estimate star formation and black hole accretion rates in distant galaxies. Using FIRESS, it will be possible to measure the [O IV] $26\mu\text{m}$ and [Ne II] $13\mu\text{m}$ fine-structure lines, and hence the BHAR and SFR in galaxies of $10^{12.5} L_{\odot}$ up to $z \sim 1.8$ and $z \sim 3$, respectively. We expect around 16000 object/deg 2 with both [O IV] $26\mu\text{m}$ and [Ne II] $13\mu\text{m}$ lines brighter than 10^{-19}W/m^2 at $z > 0.8$, with the large majority ($> 90\%$) of them securely detected in at least half of the 12 PRIMAGER bands. At the same spectroscopic depths, we expect over 2,000 object/deg 2 at $z = 1.5 - 2.5$ that could be followed-up with FIRESS to derive metallicity measurements using the [N III] $57\mu\text{m}$ and [O III] $52\mu\text{m}$ emission lines. When combined with measures of the PAH emission features, easily detectable with FIRESS at $z > 2$, it will be possible to study the connection between small grain emission and gas metal abundance in thousands of distant galaxies.

Finally, we have used the models and correlations between bolometric luminosity and outflow mass and velocity seen in the local Universe, to predict that with a modest amount of observing time, it will be possible to detect and characterise the galactic outflows with the high-res mode of FIRESS, using the OH molecular absorption feature, in more than 200 galaxies to $z \sim 1 - 2$. These observations will expand, by nearly an order of magnitude, the number of galactic outflows measured in the far-IR and allow us to test whether such outflows are sufficient to quench star-formation in bright IR galaxies over the past 10 Gyr of cosmic time.

Acknowledgements. The authors acknowledge the scientific help of John Arballo and the PRIMAGER extragalactic science working groups. LB acknowledges support from INAF under the Large Grant 2022 funding scheme (project "MeerKAT and LOFAR Team up: a Unique Radio Window on Galaxy/AGN co-Evolution"). LC acknowledges support from the french government under the France 2030 investment plan, as part of the Initiative d'Excellence d'Aix-Marseille Université – A*MIDEX AMX-22-RE-AB-101. RJW acknowledges support from the European Research Council via ERC Consolidator Grant KETJU (no. 818930).

References

- Akiyama, M., He, W., Ikeda, H., et al. 2018, PASJ, 70, S34
Aniano, G., Draine, B. T., Hunt, L. K., et al. 2020, ApJ, 889, 150

- Armus, L., Bernard-Salas, J., Spoon, H. W. W., et al. 2006, *ApJ*, 640, 204
- Armus, L., Charmandaris, V., Bernard-Salas, J., et al. 2007, *ApJ*, 656, 148
- Armus, L., Charmandaris, V., Spoon, H. W. W., et al. 2004, *ApJS*, 154, 178
- Armus, L., Lai, T., U, V., et al. 2023, *ApJ*, 942, L37
- Arnouts, S., Walcher, C. J., Le Fèvre, O., et al. 2007, *A&A*, 476, 137
- Baselmans, J. 2012, *Journal of Low Temperature Physics*, 176, 292
- Beare, R., Brown, M. J. I., Pimblett, K., & Taylor, E. N. 2019, *ApJ*, 873, 78
- Bernard Salas, J., Pottasch, S. R., Beintema, D. A., & Wesselius, P. R. 2001, *A&A*, 367, 949
- Berta, S., Lutz, D., Santini, P., et al. 2013, *A&A*, 551, A100
- Béthermin, M., Bolatto, A. D., Boulanger, F., et al. 2024, *subm. to A&A*, arXiv:2404.04320
- Béthermin, M., Wu, H.-Y., Lagache, G., et al. 2017, *A&A*, 607, A89
- Bianchi, S., De Vis, P., Viaene, S., et al. 2018, *A&A*, 620, A112
- Bisigello, L., Gandolfi, G., Grazian, A., et al. 2023, *A&A*, 676, A76
- Bisigello, L., Gruppioni, C., Feltre, A., et al. 2021, *A&A*, 651, A52
- Bisigello, L., Vallini, L., Gruppioni, C., et al. 2022, *A&A*, 666, A193
- Bonato, M., De Zotti, G., Leisawitz, D., et al. 2019, *PASA*, 36, e017
- Boquien, M., Burgarella, D., Roehly, Y., et al. 2019, *A&A*, 622, A103
- Brightman, M. & Nandra, K. 2011, *MNRAS*, 413, 1206
- Calzetti, D., Kennicutt, R. C., Engelbracht, C. W., et al. 2007, *ApJ*, 666, 870
- Chabrier, G. 2003, *PASP*, 115, 763
- Chartab, N., Cooray, A., Ma, J., et al. 2022, *Nature Astronomy*, 6, 844
- Ciesla, L., Boquien, M., Boselli, A., et al. 2014, *A&A*, 565, A128
- Ciesla, L., Charmandaris, V., Georgakakis, A., et al. 2015, *A&A*, 576, A10
- Cirasuolo, M., McLure, R. J., Dunlop, J. S., et al. 2007, *MNRAS*, 380, 585
- Croom, S. M., Richards, G. T., Shanks, T., et al. 2009, *MNRAS*, 399, 1755
- da Cunha, E., Charlot, S., & Elbaz, D. 2008, *MNRAS*, 388, 1595
- Dale, D. A., Smith, J. D. T., Armus, L., et al. 2006, *ApJ*, 646, 161
- Day, P. K., Cothard, N. F., Albert, C., et al. 2024, *arXiv e-prints*, arXiv:2404.10246
- Day, P. K., LeDuc, H. G., Mazin, B. A., Vayonakis, A., & Zmuidzinas, J. 2003, *Nature*, 425, 817
- De Looze, I., Cormier, D., Lebouteiller, V., et al. 2014, *A&A*, 568, A62
- Delvecchio, I., Gruppioni, C., Pozzi, F., et al. 2014, *MNRAS*, 439, 2736
- Díaz-Santos, T., Armus, L., Charmandaris, V., et al. 2013, *ApJ*, 774, 68
- Donnellan, J. M. S., Oliver, S. J., Béthermin, M., et al. 2024, *subm. to A&A*, arXiv:2404.06935
- Draine, B. T. 2003, *ARA&A*, 41, 241
- Draine, B. T. 2011, *Physics of the Interstellar and Intergalactic Medium*
- Draine, B. T., Aniano, G., Krause, O., et al. 2014, *ApJ*, 780, 172
- Draine, B. T., Dale, D. A., Bendo, G., et al. 2007, *ApJ*, 663, 866
- Dwek, E. & Cherchneff, I. 2011, *ApJ*, 727, 63
- Engelbracht, C. W., Gordon, K. D., Rieke, G. H., et al. 2005, *ApJ*, 628, L29
- Euclid Collaboration: Bisigello, L., Massimo, M., Tortora, C., et al. 2024, *subm. to A&A*
- Feltre, A., Charlot, S., & Gutkin, J. 2016, *MNRAS*, 456, 3354
- Feltre, A., Gruppioni, C., Marchetti, L., et al. 2023, *A&A*, 675, A74
- Ferland, G. J., Porter, R. L., van Hoof, P. A. M., et al. 2013, *Rev. Mexicana Astron. Astrofis.*, 49, 137
- Fernández-Ontiveros, J. A., Armus, L., Baes, M., et al. 2017, *PASA*, 34, e053
- Fernández-Ontiveros, J. A., Spinoglio, L., Pereira-Santaella, M., et al. 2016, *ApJS*, 226, 19
- Ferrarese, L. 2002, *ApJ*, 578, 90
- González-Alfonso, E., Fischer, J., Graciá-Carpio, J., et al. 2014, *A&A*, 561, A27
- González-Alfonso, E., Fischer, J., Spoon, H. W. W., et al. 2017, *ApJ*, 836, 11
- Greene, J. E., Labbe, I., Goulding, A. D., et al. 2023, *subm. to ApJ*, arXiv:2309.05714
- Gruppioni, C., Berta, S., Spinoglio, L., et al. 2016, *MNRAS*, 458, 4297
- Gruppioni, C., Béthermin, M., Loiacono, F., et al. 2020, *A&A*, 643, A8
- Gruppioni, C., Calura, F., Pozzi, F., et al. 2015, *MNRAS*, 451, 3419
- Gruppioni, C., Pozzi, F., Andreani, P., et al. 2010, *A&A*, 518, L27
- Gruppioni, C., Pozzi, F., Rodighiero, G., et al. 2013, *MNRAS*, 432, 23
- Gültekin, K., Cackett, E. M., Miller, J. M., et al. 2009, *ApJ*, 706, 404
- Habouzit, M., Li, Y., Somerville, R. S., et al. 2021, *MNRAS*, 503, 1940
- Habouzit, M., Pisani, A., Goulding, A., et al. 2020, *MNRAS*, 493, 899
- Harikane, Y., Zhang, Y., Nakajima, K., et al. 2023, *ApJ*, 959, 39
- Herrera-Camus, R., Bolatto, A., Smith, J. D., et al. 2016, *ApJ*, 826, 175
- Hickox, R. C. & Alexander, D. M. 2018, *ARA&A*, 56, 625
- Hirschmann, M., Somerville, R. S., Naab, T., & Burkert, A. 2012, *MNRAS*, 426, 237
- Hopkins, P. F., Richards, G. T., & Hernquist, L. 2007, *ApJ*, 654, 731
- Huertas-Company, M., Bernardi, M., Pérez-González, P. G., et al. 2016, *MNRAS*, 462, 4495
- Hunter, D. A., Elmegreen, B. G., & Ludka, B. C. 2010, *AJ*, 139, 447
- Hurley, P. D., Oliver, S., Betancourt, M., et al. 2017, *MNRAS*, 464, 885
- Inami, H., Armus, L., Charmandaris, V., et al. 2013, *ApJ*, 777, 156
- Kennicutt, R. C. & Evans, N. J. 2012, *ARA&A*, 50, 531
- Killi, M., Watson, D., Brammer, G., et al. 2023, *subm. to A&A*, arXiv:2312.03065
- Kirkpatrick, A., Pope, A., Sajina, A., et al. 2015, *ApJ*, 814, 9
- Klypin, A., Yepes, G., Gottlöber, S., Prada, F., & Heß, S. 2016, *MNRAS*, 457, 4340
- Kocevski, D. D., Finkelstein, S. L., Barro, G., et al. 2024, *subm. to ApJ*, arXiv:2404.03576
- Kocevski, D. D., Onoue, M., Inayoshi, K., et al. 2023, *ApJ*, 954, L4
- Kormendy, J. & Ho, L. C. 2013, *ARA&A*, 51, 511
- La Caria, M. M., Vignali, C., Lanzuisi, G., Gruppioni, C., & Pozzi, F. 2019, *MNRAS*, 487, 1662
- Lai, T. S. Y., Armus, L., U, V., et al. 2022, *ApJ*, 941, L36
- Lai, T. S. Y., Smith, J. D. T., Baba, S., Spoon, H. W. W., & Imanishi, M. 2020, *ApJ*, 905, 55
- Lamarche, C., Smith, J. D., Kreckel, K., et al. 2022, *ApJ*, 925, 194
- Lanzuisi, G., Perna, M., Delvecchio, I., et al. 2015, *A&A*, 578, A120
- Larson, R. L., Finkelstein, S. L., Kocevski, D. D., et al. 2023, *ApJ*, 953, L29
- Madau, P. & Dickinson, M. 2014, *ARA&A*, 52, 415
- Magnelli, B., Popesso, P., Berta, S., et al. 2013, *A&A*, 553, A132
- Magorrian, J., Tremaine, S., Richstone, D., et al. 1998, *ApJ*, 115, 2285
- Maiolino, R., Risaliti, G., Signorini, M., et al. 2024, *subm. to A&A*, arXiv:2405.00504
- Maiolino, R., Scholtz, J., Curtis-Lake, E., et al. 2023, *subm. to A&A*, arXiv:2308.01230
- Malek, K., Buat, V., Roehly, Y., et al. 2018, *A&A*, 620, A50
- Matthee, J., Naidu, R. P., Brammer, G., et al. 2024, *ApJ*, 963, 129
- McConnell, N. J., Ma, C.-P., Gebhardt, K., et al. 2011, *Nature*, 480, 215
- McGreer, I. D., Jiang, L., Fan, X., et al. 2013, *ApJ*, 768, 105
- Mignoli, M., Feltre, A., Bongiorno, A., et al. 2019, *A&A*, 626, A9
- Moffett, A. J., Ingarfield, S. A., Driver, S. P., et al. 2016, *MNRAS*, 457, 1308
- Moullet, A., Kataria, T., Lis, D., et al. 2023, *arXiv e-prints*, arXiv:2310.20572
- Mullaney, J. R., Daddi, E., Béthermin, M., et al. 2012, *ApJ*, 753, L30
- Nagao, T., Maiolino, R., Marconi, A., & Matsuhara, H. 2011, *A&A*, 526, A149
- Onoue, M., Inayoshi, K., Ding, X., et al. 2023, *ApJ*, 942, L17
- Peimbert, A. & Peimbert, M. 2010, *ApJ*, 724, 791
- Peng, B., Lamarche, C., Stacey, G. J., et al. 2021, *ApJ*, 908, 166
- Pereira-Santaella, M., Rigopoulou, D., Farrah, D., Lebouteiller, V., & Li, J. 2017, *MNRAS*, 470, 1218
- Pérez-González, P. G., Barro, G., Annunziatella, M., et al. 2023, *ApJ*, 946, L16
- Pérez-González, P. G., Barro, G., Rieke, G. H., et al. 2024, *accepted in ApJ*, arXiv:2401.08782
- Pilyugin, L. S., Grebel, E. K., & Kniazev, A. Y. 2014, *AJ*, 147, 131
- Polletta, M., Tajer, M., Maraschi, L., et al. 2007, *ApJ*, 663, 81
- Reines, A. E. & Volonteri, M. 2015, *ApJ*, 813, 82
- Rieke, G. H., Alonso-Herrero, A., Weiner, B. J., et al. 2009, *ApJ*, 692, 556
- Rigby, J. R., Diamond-Stanic, A. M., & Aniano, G. 2009, *ApJ*, 700, 1878
- Rodighiero, G., Bisigello, L., Iani, E., et al. 2023, *MNRAS*, 518, L19
- Ross, N. P., McGreer, I. D., White, M., et al. 2013, *ApJ*, 773, 14
- Sandstrom, K. M., Bolatto, A. D., Bot, C., et al. 2012, *ApJ*, 744, 20
- Schindler, J.-T., Fan, X., McGreer, I. D., et al. 2019, *ApJ*, 871, 258
- Schreiber, C., Elbaz, D., Pannella, M., et al. 2018, *A&A*, 609, A30
- Shimizu, T. T., Mushotzky, R. F., Meléndez, M., et al. 2017, *MNRAS*, 466, 3161
- Shivaei, I., Alberts, S., Florian, M., et al. 2024, *subm. to A&A*, arXiv:2402.07989
- Smith, J. D. T., Draine, B. T., Dale, D. A., et al. 2007, *ApJ*, 656, 770
- Somerville, R. S., Hopkins, P. F., Cox, T. J., Robertson, B. E., & Hernquist, L. 2008, *MNRAS*, 391, 481
- Somerville, R. S. & Kolatt, T. S. 1999, *MNRAS*, 305, 1
- Somerville, R. S., Olsen, C., Yung, L. Y. A., et al. 2021, *MNRAS*, 502, 4858
- Somerville, R. S., Popping, G., & Trager, S. C. 2015, *MNRAS*, 453, 4337
- Somerville, R. S. & Primack, J. R. 1999, *MNRAS*, 310, 1087
- Speagle, J. S., Steinhardt, C. L., Capak, P. L., & Silverman, J. D. 2014, *ApJS*, 214, 15
- Spilker, J. S., Phadke, K. A., Aravena, M., et al. 2023, *Nature*, 618, 708
- Spinoglio, L., Fernández-Ontiveros, J. A., & Malkan, M. A. 2022, *ApJ*, 941, 46
- Spinoglio, L., Pereira-Santaella, M., Dasyra, K. M., et al. 2015, *ApJ*, 799, 21
- Spoon, H. W. W., Armus, L., Marshall, J. A., et al. 2009, *ApJ*, 693, 1223
- Spoon, H. W. W., Farrah, D., Lebouteiller, V., et al. 2013, *ApJ*, 775, 127
- Stalewski, M., Ricci, C., Ueda, Y., et al. 2016, *MNRAS*, 458, 2288
- Stierwalt, S., Armus, L., Charmandaris, V., et al. 2014, *ApJ*, 790, 124
- Stone, M., Pope, A., McKinney, J., et al. 2022, *ApJ*, 934, 27
- Stone, M., Veilleux, S., Meléndez, M., et al. 2016, *ApJ*, 826, 111
- Talia, M., Cimatti, A., Giulietti, M., et al. 2021, *ApJ*, 909, 23
- Traina, A., Gruppioni, C., Delvecchio, I., et al. 2024, *A&A*, 681, A118
- Vallini, L., Gallerani, S., Ferrara, A., Pallottini, A., & Yue, B. 2015, *ApJ*, 813, 36
- Veilleux, S., Maiolino, R., Bolatto, A. D., & Aalto, S. 2020, *A&A Rev.*, 28, 2
- Veilleux, S., Meléndez, M., Sturm, E., et al. 2013, *ApJ*, 776, 27
- Whitcomb, C. M., Sandstrom, K., Leroy, A., & Smith, J. D. T. 2023, *ApJ*, 948, 88
- Witstok, J., Shivaei, I., Smit, R., et al. 2023, *Nature*, 621, 267
- Wright, R. J., Somerville, R. S., Lagos, C. d. P., et al. 2024, *subm. to MNRAS*, arXiv:2402.08408
- Yang, G., Boquien, M., Brandt, W. N., et al. 2022, *ApJ*, 927, 192

- Yang, G., Boquien, M., Buat, V., et al. 2020, MNRAS, 491, 740
- Yang, S. & Lidz, A. 2020, MNRAS, 499, 3417
- Yue, M., Eilers, A.-C., Ananna, T. T., et al. 2024, arXiv e-prints, arXiv:2404.13290
- Yung, L. Y. A., Somerville, R. S., Ferguson, H. C., et al. 2022, MNRAS, 515, 5416
- Yung, L. Y. A., Somerville, R. S., Finkelstein, S. L., et al. 2023, MNRAS, 519, 1578
- Yung, L. Y. A., Somerville, R. S., Finkelstein, S. L., et al. 2021, MNRAS, 508, 2706
- Yung, L. Y. A., Somerville, R. S., Finkelstein, S. L., Popping, G., & Davé, R. 2019a, MNRAS, 483, 2983
- Yung, L. Y. A., Somerville, R. S., Popping, G., et al. 2019b, MNRAS, 490, 2855
- Zavala, J. A., Casey, C. M., Manning, S. M., et al. 2021, ApJ, 909, 165
- Zhukovska, S. 2014, A&A, 562, A76